biomimetics

MDPI

Article

An Imaging-Compatible Biomimetic Bone Model of Prostate Cancer Bone Metastasis Supports Tumour-Associated Stromal Cytokine Signalling

Alissa Reinke[1,2,3,*], Jarred Facer [1,2], Nikita Walz [1,2,3], Dinuki M. Seneviratne [1,2,3], Daniel Amaya [4], Chris Wall [2,5,6], Eliza Whiteside [3,5], Jessica Feldman [1], Paulomi (Polly) Burey [1,7] and Louisa C. E. Windus [1,2,3,*]

1 SIMPLE Hub, Centre for Future Materials, University of Southern Queensland, Toowoomba, QLD 4350, Australia; nikita.walz@unisq.edu.au (N.W.); dinuki.seneviratne@unisq.edu.au (D.M.S.); jessica.feldman@unisq.edu.au (J.F.); polly.burey@unisq.edu.au (P.B.)
2 School of Health, Psychological and Medical Sciences, University of Southern Queensland, Toowoomba, QLD 4350, Australia
3 Institute of Health, University of Southern Queensland, Toowoomba, QLD 4350, Australia; e.whiteside@uq.edu.au
4 Translational Research Institute, Brisbane, QLD 4102, Australia
5 Rural Clinical School, Faculty of Health, Medicine, and Behavioural Sciences, The University of Queensland, Toowoomba, QLD 4350, Australia
6 Department of Orthopaedics, Toowoomba Hospital, Darling Downs Health, Toowoomba, QLD 4350, Australia
7 School of Science, Engineering, and Digital Technologies, University of Southern Queensland, Toowoomba, QLD 4350, Australia
* Correspondence: alissa.reinke@unisq.edu.au (A.R.); louisa.windus@unisq.edu.au (L.C.E.W.)

Abstract

Bone metastatic prostate cancer remains a major clinical challenge due to the lack of physiologically relevant models that are compatible with high-throughput drug discovery workflows. Conventional two-dimensional (2D) culture systems enable scalable, reproducible screening but fail to recapitulate the structural, mechanical and biological complexity of the bone metastatic niche. Here, we developed a biomimetic eggshell-chitosan-poly (ethylene glycol) diacrylate (EC-PEGDA) scaffold designed to support three-dimensional (3D) investigation of prostate cancer-associated tumour–stroma interactions within a bone mimetic microenvironment, while remaining compatible with standard multiwell formats and confocal imaging. Micro-computed tomography (MicroCT) and SEM demonstrated that the scaffold possessed a biologically relevant bone volume/total volume (BV/TV; 91.75 ± 1.219). Biological evaluation demonstrated cytocompatibility with multiple cell lines associated with the metastatic niche, including PC-3, LNCaP, HS-5 and hFOB1.19 cells. Distinct morphologies and multicellular spheroids were identified within the scaffolds, and osteoblastic activity was observed but was reduced when co-cultured with PC-3 cells, consistent with metastatic tumour–bone interactions. Importantly, the model supported tumour–stroma cytokine signalling, with elevated net concentrations of GM-CSF, IL-1β and TNF-α observed in HS-5-containing cultures exposed to PC-3-conditioned media. These findings indicate cytokine responses associated with tumour-derived soluble factors within the bone-mimetic microenvironment. Conditioned media studies demonstrated that tumour-derived soluble factors were sufficient to promote increased cytokine concentrations in the absence of direct cell–cell contact. Collectively, these findings demonstrate that the EC-PEGDA scaffold provides an imaging-compatible and structurally relevant bone-mimetic microenvironment capable of supporting multicellular culture and tumour-associated cytokine signalling. While the model does not fully reproduce the complexity of metastatic bone disease, it captures key aspects of tumour–stroma communications and provides a reproducible platform for investigating mechanisms relevant to prostate cancer progression within the bone.

Check for updates

Academic Editor: Hermann Ehrlich

Received: 15 October 2026
Revised: 11 November 2026
Accepted: 11 November 2026
Published: 16 November 2026

Copyright: © 2026 by the authors. Licensee MDPI, Basel, Switzerland. This article is an open access article distributed under the terms and conditions of the Creative Commons Attribution (CC BY) license.

Keywords: bone metastasis; prostate cancer; 3D scaffold; cytokine signalling; tumour microenvironment

1. Introduction

Despite significant advances in drug discovery, attrition rates remain high, with lack of efficacy being the most common cause of late-stage clinical trial failure [1,2]. Since 2013, phase II clinical trials terminated due to lack of efficacy increased from 17% to 19%, while 35% of phase III trials were terminated [3]. The average three-year cost of developing a new drug has risen to $3.7 billion USD, compared to $0.86 billion two decades ago, yet there has been no evidence of improved efficacy of late-stage trials [4]. These trends highlight the fundamental disconnect between the conventional pre-clinical drug discovery pipeline and physiologically relevant models. Beyond scientific and economic considerations, there is also increasing emphasis on the principles of Replacement, Reduction and Refinement (3Rs), which seek to minimise animal use in research through the development of more predictive alternative models.

Historically the drug discovery pipeline has relied on two-dimensional (2D) cell culture due to low variability, scalability and compatibility with high-throughput screening (HTS) [5,6]. While these are all important considerations, biological relevance is also crucial for moving drugs successfully through the drug discovery pipeline, and 2D culture lacks the biological, structural and mechanical complexity found in the cancerous, or metastatic, niche [7,8]. This significant limitation results in poor screening outcomes and inefficient resource allocation within the pipeline.

Three-dimensional (3D) cell culture models, often hydrogels, have emerged over the last two decades, with the most recent advancement being the use of patient-derived organoids [9–12]. While hydrogels have been instrumental in the development of 3D culture, the mechanotransduction cues provided by many hydrogel systems do not fully replicate those of the rigid, mineralised bone environment. Other approaches, including multicellular spheroids, organoids and bioprinted models, offer increasing levels of cellular and spatial complexity but present different trade-offs between biological fidelity, reproducibility, imaging accessibility, scalability and integration with automated workflows. Spheroid-based approaches can reproduce aspects of 3D cell–cell interactions but lack the structural and mineral characteristics of native bone, while more complex bioprinted and organoid systems can better reproduce spatial heterogeneity but may introduce greater technical complexity and inter-sample variability. Therefore, no single existing approach fully resolves the competing requirements for bone-relevant structural and mechanical properties, cellular complexity, reproducibility and compatibility with scalable drug-screening workflows.

Despite these advances, many existing bone-mimetic models remain limited by poor imaging accessibility, complex fabrication protocols, restricted scalability and inadequate compatibility with routine laboratory workflows. Increasing biological complexity is frequently accompanied by reduced reproducibility, more demanding analytical requirements and challenges integrating with automated screening systems. Consequently, there remains a need for reproducible bone-mimetic culture systems that permit direct visualisation of tumour–stroma interactions while retaining biologically relevant structural characteristics of bone.

Despite substantial advances in organoid and 3D culture technologies since the original studies in 2009 [13], widespread adoption within high-throughput drug screening workflows remains limited due to challenges associated with reproducibility, cost, scalability and automation. A recent systematic review investigating in vitro models for bone metastatic cancers highlighted that models are often opaque, requiring sectioning in order to visualise cells, which is not compatible with longitudinal or scalable imaging workflows [14]. Many

existing 3D models lack the structural integrity required for integration with robotics and standard multiwell formats. The preselection of similar sized spheroids is frequently used to improve reproducibility and compatibility with high-throughput workflows [15,16]. This creates fundamental trade-offs, as physiologically relevant models can require additional manipulation or preselection to achieve the consistency required for high-throughput analysis, potentially introducing selection bias, whereas highly standardised HTS-compatible systems may sacrifice aspects of biological fidelity.

These limitations create an opportunity for bone-mimetic platforms that retain sufficient structural integrity for routine handling and standard multiwell culture while also permitting direct imaging without destructive sectioning. Rather than attempting to reproduce every feature of the metastatic niche, such platforms may provide an intermediate level of model complexity between conventional spheroid/hydrogel systems and technically intensive organoid or bioprinted approaches. While patient-derived organoids provide greater patient specificity and heterogeneity [10,17], their cost, variability and technical complexity can present challenges for standardisation and scalable screening. The present approach is therefore intended as an intermediate platform that combines greater microenvironmental relevance than conventional cell culture with the reproducibility and accessibility required for systematic model development and future screening optimisation. Importantly, compatibility with multiwell formats and non-destructive imaging provides a foundation for future optimisation toward automated, higher-throughput drug-screening workflows.

The convergence of HTS and artificial intelligence (AI)-driven analytics has the potential to significantly enhance drug discovery systems, particularly through imaging-based phenotypic screening of 3D environments, which is a rapidly growing technique within the pipeline [18]. Machine learning enables automated pattern recognition and predictive modelling, which could be used to analyse complex datasets, identifying subtle changes and drug response signatures previously unnoticed [19]. This integration supports iterative discovery workflows, where phenotypic outputs continuously refine predictive models, accelerating hypothesis generation and optimisation [20]. Many studies have stated compatibility with the drug discovery pipeline [21–23], yet provide limited evidence demonstrating platform reproducibility or scalability under screening conditions. Consequently, claims of HTS compatibility do not necessarily demonstrate readiness for fully automated high-throughput screening. These limitations are particularly evident in diseases where cell–microenvironment interactions drive disease progression, such as metastatic cancers of bone [24].

Bone metastatic cancers present a major clinical challenge for advanced-stage cancers, particularly prostate cancer, with approximately 30% of prostate cancer patients developing skeletal involvement [25,26]. It is widely accepted that the bone metastatic niche is unique and complex, with a dynamic interplay between many cell types, including osteoblasts, osteoclasts, bone stromal cells, immune cells and the mineralised extracellular matrix [27,28]. In recent decades, priming of the premetastatic niche has become a prominent area of research [24,29]. This phenomenon suggests that circulating soluble factors such as cytokines and chemokines, released by the primary tumour, can influence the behaviour of cells in the premetastatic niche and prime them for the arrival of tumour cells, essentially creating an immunosuppressive environment that will support the growth of bone metastases. This explains why tumour cells circulate systemically, yet often only colonise specific sites, with bone being a common site of metastasis for prostate cancer. This bone metastatic microenvironment drives a vicious cycle of bone remodelling and tumour growth, ultimately leading to disease progression. This progression is highly specific to the local microenvironment and has historically been difficult to replicate in pre-clinical models.

As cytokine signalling is a key mediator of tumour–stroma communication and is implicated in premetastatic niche development, evaluating cytokine profiles within 3D systems is important in determining whether these models support biologically relevant signalling environments. Bone-mimetic models that can combine these biological interactions with structural stability and imaging accessibility may therefore help bridge the gap between simplistic early-stage assays and resource-intensive in vivo studies. However, their value for drug discovery depends not only on biological relevance but also on demonstrating reproducibility, compatibility with standard culture formats and the capacity for future integration with automated analytical workflows. HTS-compatible bone models bridge the gap between simplistic early-stage assays and resource-intensive in vivo studies. By developing a more predictive in vitro platform, the pre-clinical model could enable improved identification of appropriate therapeutic compounds specific for the metastatic bone niche.

Bone-mimetic scaffold design requires a balance between biological relevance, structural stability and reproducibility. Chitosan was selected as a naturally derived polysaccharide due to its biocompatibility, porous architecture and ability to support cell attachment and tissue-like growth. Poly (ethylene glycol) diacrylate (PEGDA) was incorporated to provide tuneable crosslinking and mechanical stability, improving scaffold robustness and consistency for routine handling and imaging applications. Eggshell-derived calcium carbonate was included as a sustainable mineral source to introduce bone-relevant inorganic components and support the development of a more physiologically representative microenvironment. The combination of these materials was therefore intended to integrate the biological advantages of a natural polymer with the structural control afforded by a synthetic polymer and the mineral characteristics of bone tissue. Accordingly, this study developed and characterised a solid, biomimetic model, capable of supporting relevant tumour–stroma interactions within a bone-mimetic microenvironment while remaining compatible with standard multiwell handling and imaging-based analysis. These characteristics provide a foundation for future optimisation toward automated drug-screening applications, rather than assuming immediate HTS readiness, facilitating translationally relevant evaluation of therapeutic candidates.

2. Methods

2.1. Scaffold Preparation

2.1.1. Eggshell Preparation

Commercially available cage-free eggs (Sunny Queen, Carole Park, QLD, Australia) were cracked, and the shells were stored under refrigeration for no longer than 48 h. The eggshells were then rinsed with distilled water, followed by sequential washing in 70% ethanol and 2% acetic acid. After washing, the shells were dried overnight at room temperature. The dried shells were milled using a 2 L gear-driven planetary ball mill (Across International, Bayswater, VIC, Australia) with 20 mm ceramic balls for six hours. The resulting material was then dried overnight in an oven at 200 °C. Finally, the powder was sieved to obtain particles smaller than 150 µm using a test sieve shaker (Endecott's, Hope Valley, UK).

2.1.2. 3D-Printed Mould

A 3D-printed mould was developed to produce cylindrical scaffolds that fit in standard 96- and 384-well plates. Scaffolds for the 96-well plates were 5.3 mm in diameter and 1.5 mm in height. Scaffolds for the 384-well plates were 2 mm × 2 mm and 1.5 mm in height. The scaffold mould was designed in Autodesk Fusion 360 (v.2706.1.17, San Francisco, CA, USA). The completed model was sliced in Ultimaker Cura 5.5.0 (UltiMaker, KS Zaltbommel, Netherlands, 2023) and printed using polylactic acid filament (PolyTerra, PLA™, Polymaker,

Changshu, China) with 15% infill, with a 0.2 mm layer height using a Bambu Labs X1 Carbon 3D printer (Bambu Labs, Shenzhen, China).

2.1.3. Scaffold Design

Scaffolds were fabricated using a composite mixture of chitosan, poly (ethylene glycol) diacrylate (PEGDA), eggshell powder, and Irgacure 2959. Chitosan (98% deacetylated, Sigma-Aldrich, Burlington, MA, USA) was first dissolved in 80% acetic acid to a final concentration of 7.9% (w/v), ensuring complete dissolution prior to further additions. PEGDA (Sigma-Aldrich, USA) was then incorporated at a final concentration of 23.5% (w/v), and the mixture was thoroughly homogenised. Finely milled eggshell powder was subsequently added at 1.6% (w/v) and manually mixed into the polymeric suspension using a stainless-steel laboratory spatula under ambient laboratory conditions until a visually homogeneous dispersion was obtained. Finally, Irgacure 2959 (Sigma-Aldrich, USA) was introduced as a photo initiator at a final concentration of 0.2% (w/v). The resulting mixture was handled under light-protected conditions and cured under ultraviolet light for 5 min to induce crosslinking. The component mixture was then frozen overnight at −80 °C, before being placed into a freeze-dryer (Alpha 2-4 LDPlus, Martin Christ, Osterode am Harz, Germany) for 24 h. The scaffolds were subsequently sterilised in self-sealing pouches (Pacific Medical, Briar Hill, VIC, Australia) via autoclave under standard conditions (121 °C, 21 min). Prior to use, scaffolds were neutralised and hydrated overnight at 4 °C in phosphate-buffered saline (PBS).

2.2. Material Characterisation

2.2.1. Differential Scanning Calorimetry

Differential scanning calorimetry (DSC) was used to assess the thermal properties of the autoclaved scaffolds ($n = 8$). Measurements were performed using a calibrated DSC (TA instruments DSC25, New Castle, DE, USA) instrument within a nitrogen atmosphere. Samples were weighed at 9.5+/−1 mg for each sample and placed within aluminium DSC pans with a closed lid and heated from 25 °C to 250 °C at a rate of 10 °C/min, cooled to 25 °C and then went through a second heating cycle under the same conditions as previously stated.

2.2.2. Fourier-Transform Infrared (FT-IR) Spectroscopy

The chemical compositions of the scaffolds were evaluated using Fourier-Transform Infrared (FT-IR) spectroscopy. FT-IR spectroscopy was completed using a Thermo Scientific Nicolet iS50 FT-IR spectrophotometer (Waltham, MA, USA), with a frequency range of 400–4000 cm^{-1}. An average for each spectrum was recorded from 64 scans across five independently prepared samples and processed using OMNIC spectra software (v7.0, Thermo Scientific, Waltham, MA, USA).

2.2.3. Swelling

Autoclaved freeze-dried scaffolds ($n = 4$) were weighed dry and then assessed for their swelling capabilities through complete submersion in PBS. Water uptake was measured by weighing scaffolds at 0, 1, 2, 3, 4, 5, 10, 15, and 30 min and 24 and 48 h. Data was then processed and expressed as swelling percentage using the equation below.

$$\text{Swelling } \% = \frac{\text{Swollen weight} - \text{dry weight}}{\text{Dry weight}} \times 100$$

2.2.4. Degradation

Degradation behaviour of autoclaved scaffolds ($n = 4$ for each time point) was assessed over a four-week period. The scaffolds were initially weighed and submerged within PBS under standard cell culture conditions (37 °C and 5% CO_2) for the following time points: 24, 48 and 72 h and 1, 2, 3 and 4 weeks, with original weight and dry weight after incubation recorded. Each time point had independent material samples, as the scaffolds were left to dry for 5 days to obtain dry mass reading. Scaffold degradation was quantified as the percentage change in dry mass relative to the initial mass at each time point, using the equation below. W_0 is the initial dry weight of the scaffold prior to incubation, and W_t is the dry weight at the specified time point after incubation.

$$\text{Degradation (\%)} = \frac{\mathrm{W_0 - Wt}}{\mathrm{W_0}} \times 100$$

2.2.5. Mechanical Characterisation

Samples were tested on a TA texture analyser (TA Instruments, New Castle, DE, USA), with Exponent software v 8.0.14.0 (TA Instruments, New Castle, DE, USA) with a 100 kg load cell ($n = 3$). Scaffolds were hydrated for 24 h and were compressed at a rate of 0.1 mm/min. Elastic (Young's) modulus was calculated by the following equation, where E is elastic (Young's modulus), σ is strain, and ε is stress.

$$\mathrm{E} = \frac{\sigma}{\varepsilon}$$

Stiffness was calculated using the following equation, where k is stiffness, E is the elastic (Young's) modulus, A is the cross-sectional area (mm) and L is the length (mm). This was completed for each individual sample.

$$\mathrm{k} = \frac{\mathrm{EA}}{\mathrm{L}}$$

2.2.6. Architectural Analysis

A Skyscan 1272 benchtop microCT (Bruker, Kontich, Antwerp, Belgium) was used to characterise and analyse the structure of EC-PEGDA scaffolds in two different conditions (dry and hydrated). Dry EC-PEGDA scaffolds ($n = 3$) and hydrated EC-PEGDA scaffolds ($n = 3$) were placed directly into a 500 µL Eppendorf tube for imaging. Following water submersion, scaffolds were placed into 10 mL of Lugol's Iodine Solution (0.66% Iodine, 1.32% Potassium Iodide) for 15 min in a 15 mL falcon tube to enhance their contrast against water. The samples were then moved into a clean 500 µL Eppendorf tube with water for imaging. Scanning parameters were specific to the sample preparation and are detailed in Table 1.

Following Acquisition, the raw data was reconstructed on NRecon 2.2.0.6 (Bruker, Belgium), using a constant dynamic range, ring artifact, and beam hardening (Table 1). DataViewer 1.6.0.0 (Bruker, Belgium) was then used to check and reorientate the datasets for analysis. Sample volume (Obj.V), porosity, and structural separation was determined using CTAn 1.20.8.0 (Bruker, Belgium). New data sets were created for the pores and structural separation for creating 3D images.

Three-dimensional images were created on CTvox 3.3.0 (Bruker, Belgium). Connectivity density (Conn. D), fibre size (Tb. Sp) and degree of anisotropy were calculated using the BoneJ plugin for Fiji (ImageJ v.1.54r).

Table 1. Scanning parameters for MicroCT.

	Dry EC-PEGDA	Submerged EC-PEGDA
Acquisition		
Pixel Size (µm)	6	6
Camera binning	2 × 2	2 × 2
Voltage (kV)	50	50
Current (µA)	200	200
Exposure time (millisecond)	100	500
Filter	No	Al 0.25 mm
Rotation step (°)	0.24	0.24
Acquisition rotation (°)	360	360
Reconstruction		
Ring Artifact	5	5
Beam Hardening	40	20
Dynamic Range	Min 0.015–Max 0.100	Min 0.019–Max 0.140

2.2.7. Rheology

Rheological properties of the scaffold were characterised using an Anton Paar MCR 502 Rheometer (Anton-Paar-Strasse 20, 8054, Graz, Austria). Oscillatory shear measurements were conducted to determine storage (G′) modulus, loss (G″) modulus, and complex viscosity (η*; mPa·s) over a frequency range of 0.1–100 rad·s^{-1} ($n = 8$) at room temperature.

2.3. Biological Performance

2.3.1. Cell Culture

PC-3 (CRL-1435), LNCaP (CRL-1740), HS-5 (CRL-3611) and hFOB1.19 (CRL-3602) cells were obtained from the American Tissue Culture Collection (ATCC, Manassas, VA, USA). Hs27 (ECACC 94041901) cells were obtained from the European collection of authenticated cell cultures (ECACC, Porton Down, Salisbury UK). PC-3 and LNCaP cells were selected, as they are metastatic prostate cancer lines, with PC-3 derived from a bone metastasis and LNCaP from a lymph not metastasis. HS-5 cells are normal stromal cells found in the bone environment, while hFOB1.19 are foetal osteoblasts representing the normal osteoblastic population. Finally, HS-27 cells were selected as the control cell line. PC-3, LNCaP, HS-5 and Hs27 cells were maintained in RPMI-1640 (Sigma-Aldrich, MA, USA), supplemented with 10% foetal bovine serum (FBS; Bovogen Biologicals, Keilor East, VIC, Australia). hFOB1.19 cells were maintained in phenol red-free DMEM/F12 with 10% FBS and differentiated at the restrictive temperature (39 °C, 5% CO_2). All other cells were maintained in standard cell culture conditions (37 °C, 5% CO_2).

2.3.2. Reactive Cell Lines

Cells were grown under normal conditions, and reactive cell lines were created as per methods reported previously [12]. Briefly, conditioned media (CM) was collected from cells every 48 h when they were 60–80% confluent, spun at 300× *g* for five minutes and syringe filtered at 0.22 µm to remove cellular debris. Cells were passaged using standard RPMI +10% FBS for 24 h, before having the media changed to CM. Cells were in culture for 6 days with CM, before being used for assays. The reactive lines created are presented

in Table 2; the nomenclature for the reactive cell lines is 'cell line-CM' (e.g., PC-3-HS-5 represents PC3 cells treated with HS-5-conditioned media). For co-culture experiments, the nomenclature is cell line & cell line (i.e., PC-3 & HS-5 represents the PC-3 and HS-5 coculture). The combinations listed below represent all possible combinations of the cell lines, which allows for comparison between the contact-mediated and soluble-mediated changes that occur.

Table 2. Propagated cell lines exposed to conditioned media (CM) and their respective nomenclature for the resulting reactive cell lines. The first cell line in each designation identifies the recipient cell line, and the second identifies the cell line from which the CM was derived.

Cell Line	CM-Derived Cell Line	Reactive Cell Line Generated
PC-3	HS-5	PC-3-HS-5
	LNCaP	PC-3-LNCaP
	Hs27	PC-3-Hs27
	hFOB1.19	PC-3-hFOB1.19
HS-5	PC-3	HS-5-PC3
	LNCaP	HS-5-LNCaP
	hFOB1.19	HS-5-hFOB1.19
hFOB1.19	PC-3	hFOB1.19-PC-3
	LNCaP	hFOB1.19-LNCaP
	HS-5	hFOB1.19-HS-5
	Hs27	hFOB1.19-Hs27
LNCaP	HS-5	LNCaP-HS-5
	PC-3	LNCaP-PC-3
	hFOB1.19	LNCaP-hFOB1.19
	Hs27	LNCaP-Hs27
Hs27	PC-3	Hs27-PC-3
	LNCaP	Hs27-LNCaP
	hFOB1.19	Hs27-hFOB1.19

2.3.3. Visualisation

Scaffolds ($n = 5$) were prepared for scanning electron microscopy (SEM) to assess surface morphology and cell adhesion. PC-3 cells were cultured at a density of 1×10^5 cells/well for 7 days under standard cell culture conditions (39 °C, 5% CO_2). Specimens were fixed in 4% (w/v) paraformaldehyde for 20 min, rinsed three times with PBS, and dehydrated through a graded ethanol series (50%, 70%, 80%, 95% and 100%) for 10 min per wash at room temperature. Samples were mounted on 12.6 mm diameter aluminium pin-type stubs using conductive double-sided adhesive carbon tape. The samples were sputter-coated with 6 nm of platinum using a JEOL JEC-3000 FC Auto Fine Coater (JEOL, Akishima, Tokyo, Japan). Imaging was performed using a JEOL JSM IT800HL Schottky Field-Emission Scanning Electron Microscope (JEOL, Akishima, Tokyo, Japan).

2.3.4. Metabolic Activity

Cell viability and metabolic activity were assessed using the Alamar Blue™ assay according to the manufacturer's protocol for 4 h at 37 °C in a humidified incubator with 5% CO_2. Samples were read at 72 h ($n = 3$ biological, $n = 5$ technical). Fluorescence was measured using a VarioSkan LUX Multimode plate reader (ThermoFisher Scientific, Woolloongabba, QLD, Australia) with an excitation wavelength of 570 nm and emission wavelength of 610 nm and read with the scaffold in the well. Fluorescence was adjusted against blank wells. Data were presented as mean relative fluorescent units (RFU). For monoculture, cells were seeded at 1×10^5 cells/well (BioRad Automatic Cell counter,

Hercules, CA, USA) in a 96-well plate (Corning, Glendale, AZ, USA). For co-culture, cells were seeded at 5×10^4 cells/well for each cell type.

2.3.5. Confocal Microscopy

Cells were fixed with 4% (w/v) paraformaldehyde for 20 min at room temperature and permeabilised using 1% (w/v) bovine serum albumin (BSA) and 0.1% (v/v) Triton X-100 in PBS. Following PBS washes, samples were stained for filamentous actin (F-actin) using Invitrogen™ ReadyProbes™ Reagent F-Actin Phalloidin Conjugates according to the manufacturer's instructions (2 drops/1.5 ml; ThermoFisher Scientific, Woolloongabba, QLD, Australia). Cell nuclei were counterstained with DAPI (1 ug/mL, ThermoFisher, Australia). Z-stack images of scaffold samples were acquired for DAPI and Alexa 555 fluorescence signal on the Leica Stellaris 5 confocal system (Leica Microsystems, Wetzlar, Germany) using a 40 × objective (NA 1.25). The 3D image visualisation and analysis were performed using Imaris x64 software (v7.4.2; Zurich, Switzerland).

2.3.6. Alkaline Phosphatase Activity

The alkaline phosphatase (ALP) activity of hFOB1.19 and PC-3 cells was analysed using a kinetic ALP assay kit (MAK447; Sigma-Aldrich, USA). hFOB1.19 cells were seeded in monoculture 2D and 3D environments, while PC-3 and hFOB1.19 cells were co-cultured in 2D and 3D environments. Cells were seeded in a 96-well plate at a seeding density of 1×10^5 cells/well and incubated for 72 h. Co-culture was seeded with 5×10^4 cells/well of each type (hFOB1.19 and PC-3). Assay was undertaken as per the manufacturer's instructions, using 50 µL of sample. Absorbance was read using a VarioSkan Lux Multimode multiplate reader (ThermoFisher Scientific, Australia), at an optical density of 405 nm, with a reading taken every minute for 15 min ($n = 3$ biological, $n = 5$ technical).

2.3.7. Calcium Assay

To determine whether the scaffold supports osteoblastic differentiation and mineralisation, the calcium deposition of cells was analysed using a Sigma-Aldrich calcium assay kit (MAK477). hFOB1.19 cells were seeded in monoculture 2D and 3D environments, while PC-3 and hFOB1.19 cells were co-cultured in 2D and 3D environments. PC3 and hFOB1.19 were seeded in a 96-well plate at a density of 1×10^5 cells/well and incubated for 72 h. The assay was performed according to the manufacturer's instructions. Absorbance was read using a VarioSkan Lux multimode multiplate reader (ThermoFisher, Australia) at an optical density of 612 nm ($n = 3$ biological, $n = 5$ technical) and corrected against unseeded blank wells (2D) or scaffolds (3D).

2.3.8. High-Throughput Screening and Imaging Capability Evaluation

To evaluate assay reproducibility and compatibility with HTS workflows, inter- and intra-plate variability was determined using PC-3 cells, seeded at 10,000 cells per well, in both 2D and 3D environments as described previously ($n = 20$ per variable per plate across 3 biological repeats). Positive wells contained viable cells maintained in RPMI-1640, supplemented with 10% foetal bovine serum. Negative wells included the addition of 5% DMSO; control wells contained media only. Cells were cultured for 72 h (37 °C, 5% CO_2) before being read on a VarioSkan LUX Multimode plate reader (ThermoFisher Scientific, Australia) with an excitation wavelength of 570 nm and emission wavelength of 610 nm.

Inter- and intra-plate variability was determined by the following equation, where CV% is coefficient of variation and SD is the standard deviation.

$$\text{CV \%} = \frac{\text{SD}}{\text{mean}} \times 100$$

Z′ was determined by the following equation, where σ_p and σ_n represent the standard deviation of the positive and negative controls, respectively, and μ_p and μ_n represent the mean of the positive and negative controls, respectively.

$$Z' = 1 - \left[\frac{3\left(\sigma_p + \sigma_n\right)}{\left|\mu_p - \mu_n\right|} \right]$$

2.3.9. Cytokine Analysis

To assess tumour–stroma signalling and evaluate whether the scaffold recapitulated cytokine-driven interactions observed in the metastatic niche, a cytokine analysis was performed. A ProcartaPlex™ Human Cytokine Panel 1B 25plex (EPX250-12166-901) kit (Invitrogen Thermo Fisher, Carlsbad, CA, USA) was used and read on a Luminex xMAP (Invitrogen Thermo Fisher, USA). All procedures were followed as per the manufacturer's instructions, with samples being incubated for 60 min at room temperature, before addition of antibodies. Cell culture supernatant was collected after 72 h, with monoculture conditions having cells seeded at 1×10^5 cells/well (BioRad Automatic Cell counter) in a 96-well plate. For co-culture conditions, cells were seeded at 5×10^4 cells/well for each cell type. This was completed as 3 biological replicates and 5 technical replicates.

2.4. Statistical Analysis

All values are represented as the mean ± standard error of the mean. For cytocompatibility and cytokine testing, a Kruskal–Wallis test was performed with Dunn's post hoc testing. For ALP and calcium assays, a Welches *t*-test was completed between each group. Statistical significance was defined as a p-value < 0.05. Statistical analysis and graph generation were performed using GraphPad Prism (v10, La Jolla, CA, USA).

3. Results and Discussion

3.1. Material Characterisation

3.1.1. Differential Scanning Calorimetry

A broad endothermic peak in the region of 110–120 °C was identified in the initial run, attributed to the loss of bound water and residual acetic acid within the polymer network (Figure 1A) [30]. The use of hermetically sealed pans likely broadens this peak within the polymer network by limiting rapid evaporation and allowing interactions between the water and polymer to persist over a wider range. The magnitude of this endothermic dip in the initial run masks all other thermal transitions, prompting the inclusion of a cooling and subsequent heating run. Upon removal of the volatile compounds, the second heating run showed no glass transition, consistent with previously noted properties of chitosan [31].

These thermal characteristics provide important information regarding the thermal behaviour and stability of the scaffold in its as-fabricated state. The pronounced water retention is a relevant consideration during manufacture and sterilisation, as exposure to elevated temperatures during autoclaving may alter material properties, and understanding the thermal response of the scaffold is important when assessing whether these properties are maintained following sterilisation.

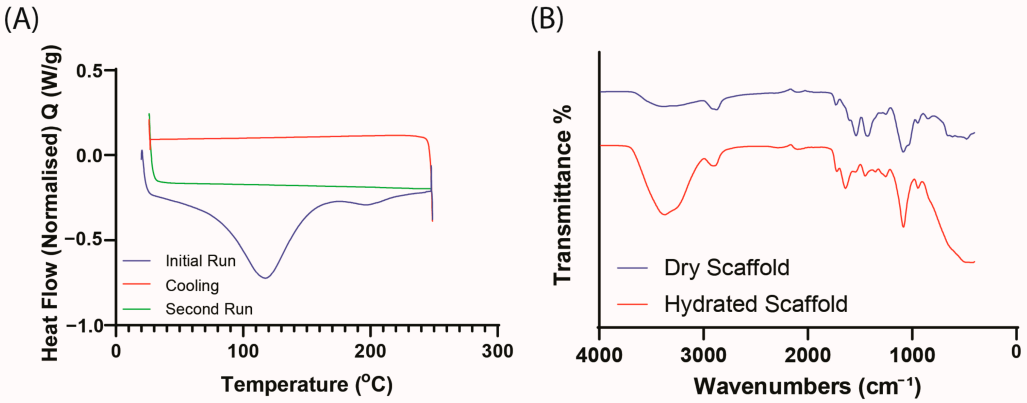


Figure 1. Thermal and chemical characterisation of EC-PEGDA scaffolds. (**A**) DSC trace of scaffolds, showing the initial run (blue), followed by a cooling phase (red), and a second heating run (green) to identify true material properties. (**B**) FT-IR spectra of dry (blue) and hydrated (red) EC-PEGDA scaffolds.

3.1.2. Fourier-Transform Infrared Spectroscopy

The FT-IR spectra (Figure 1B) of the hydrated and dry EC-PEGDA scaffolds support successful integration of chitosan and eggshell within the scaffold. The broad band observed in the region of 3200 cm^{-1}–3500 cm^{-1} can be attributed to overlapping O-H and N-H stretching vibrations, suggesting both hydroxyl and amine groups [32]. The hydrated sample has a more significant band due to the increased presence of water and hydrogen bonds within the sample. Peaks at 2900 cm^{-1} suggest C-H stretching vibrations, which could be attributed to both the chitosan and PEGDA components [33,34]. Amide I (1650 cm^{-1}) and amide II (1550 cm^{-1}) bands are present and are attributed to chitosan [33]. In the hydrated scaffold, increased intensity in the 1650 cm^{-1} region may also reflect the H-O-H bending vibration of absorbed water, which overlaps with the amide I band. Peaks in the region of 1400 cm^{-1} are carbonate groups, verifying successful incorporation of the eggshell (Calcium carbonate; $CaCO_3$) [32]. The differences in spectra peak intensity in the two test groups are strongly suggestive of hydration, with increased water evident in the hydrated sample. This further supports the DSC findings of a highly hydratable, amorphous material.

3.1.3. Swelling and Degradation Analysis

The EC-PEGDA scaffolds exhibited rapid swelling within the first five minutes, followed by a plateau phase and slight reduction in fluid uptake over time (Figure 2A). This behaviour is consistent with initial polymer hydration followed by network relaxation. Importantly, the rapid equilibrium suggests that scaffolds reach a stable hydrated state suitable for reproducible cell culture prior to seeding. Similarly, degradation studies show limited degradation until the four-week time point, suggesting long-term cell culture assays are feasible without scaffold breakdown (Figure 2B).

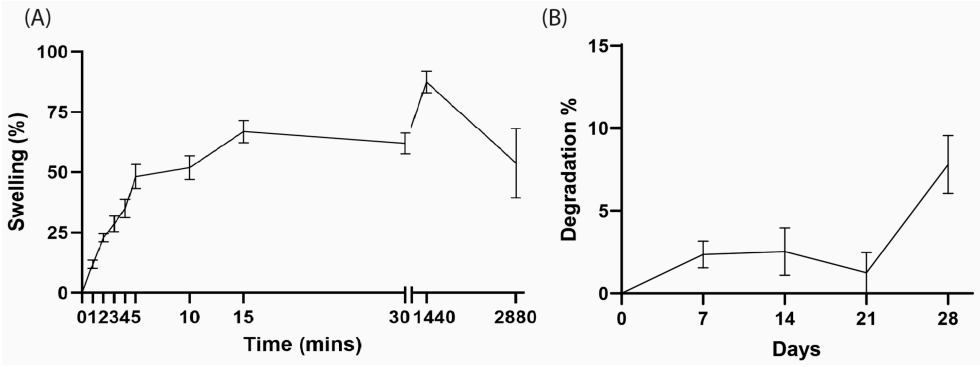


Figure 2. Swelling and degradation behaviour of EC-PEGDA scaffolds. (**A**) Swelling profile of EC-PEGDA scaffold over a 48 h period ($n = 4$). (**B**) Degradation profile over a four-week period ($n = 4$).

3.1.4. Mechanical Characterisation and Architectural Analysis

Mechanical analysis of hydrated scaffolds revealed a Young's modulus of 178.00 ± 5.50 MPa and a stiffness of 3907.00 ± 345.00 N/mm (Table 3), confirming the scaffold maintains structural capacity in an appropriate range representative of trabecular bone [35–38]. Importantly, these results are completed in hydrated scaffolds, with dry scaffolds often showing different mechanical properties, despite the end use being in a hydrated state, a distinction not often reported when looking at mechanical properties [14]. The maintained stiffness in a hydrated state is essential for replicating the bone microenvironment, with trabecular bone being a stiffer environment than a conventional hydrogel.

Table 3. Mechanical properties and microarchitecture of EC-PEGDA scaffolds.

Variable	EC-PEGDA Scaffold	Trabecular Bone
Ultimate compressive strength (MPa)	1.53 ± 0.58	0.1–30
Young's Modulus (MPa)	178.00 ± 5.50	17,900–18,160
Stiffness (N/mm)	3907.00 ± 345.00	236
BV/TV	91.75 ± 1.219	45–95
Tb. Sp. (µm)	107.5 ± 25.23	226 ± 29
Tb. Th. (µm)	440.0 ± 84.70	125.8
Conn D.	$1.24 \times 10^{-8} \pm 4.11 \times 10^{-9}$	$1.1 \times 10^{-8} \pm 0.7 \times 10^{-8}$
Degree of Anisotropy	0.58 ± 0.05	0.554 ± 0.067

BV/TV: Bone volume/Total volume; Tb. Sp.: spacing of pores; Tb. Th.: spacing between pores; Conn. D.: connectivity density.

While it is standard to report ultimate compressive strength (1.53 ± 0.58MPa), this is not strictly relevant for in vitro cell culture, as culture is generally not completed under active compression; rather, the cells experience, and respond to, the stiffness of a material [14]. It is possible to create culture conditions where cells are compressed with pistons to evaluate their response [39]; however, this is highly specialised and largely underutilised, especially in HTS workflows.

The architecture of a scaffold is equally important to ensure appropriate cellular growth. EC-PEGDA scaffolds exhibited a porous structure (Figure 3A,B), with a BV/TV of 91.75 ± 1.219% in the range of 45–95% [40]. BV/TV alone does not give perfect insight into architecture, as there may be many small pores, creating a large porosity, or a few large pores. Of note, the hydrated scaffold pore distribution and size was altered by hydration status, with the hydrated scaffolds having pores large enough to allow cellular infiltration

(107.5 ± 25.23 µm; Figure 3C–F) [41]. Other key parameters include the degree of anisotropy, which shows the variation of trabecular bone depending on the direction viewed, and the trabecular thickness and spacing. Human trabecular bone naturally has variation between patients, with trabecular thickness being reported as 125.8 µm, trabecular spacing being 226 ± 29 µm and Conn. D being $1.1 \times 10^{-8} \pm 0.7 \times 10^{-8}$ [42]. Trabecular thickness in the current model is larger than that found in bone (440.0 ± 84.70 µm); however, the connectivity density (Conn. D.; $1.24 \times 10^{-8} \pm 4.11 \times 10^{-8}$) and degree of anisotropy (DA; 0.58 ± 0.05) is within the range found in human bone (0.554 ± 0.067 [43]).

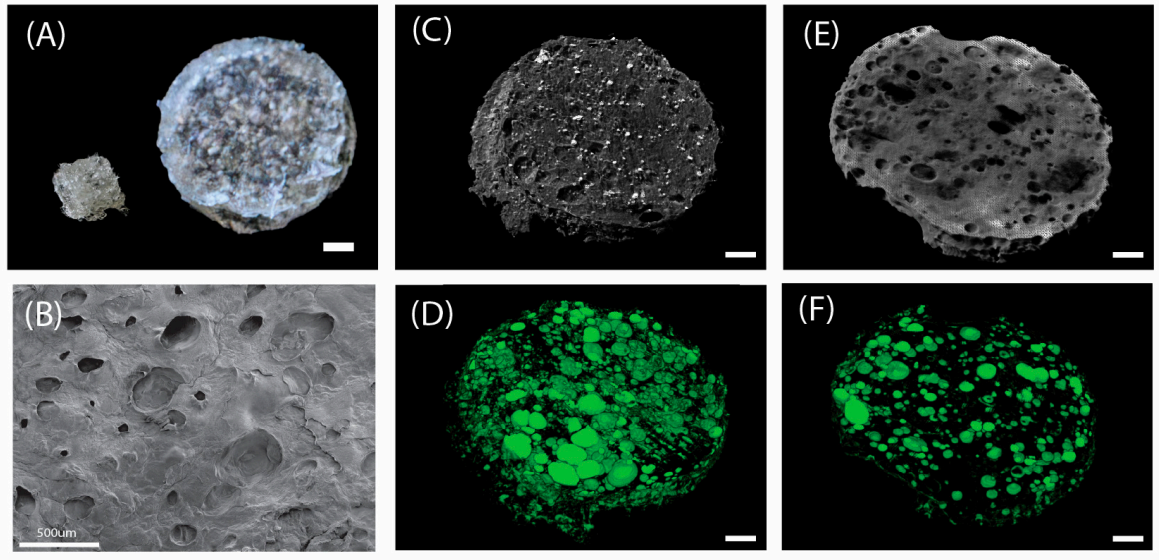


Figure 3. Macroscopic appearance, surface morphology and microarchitecture of EC-PEGDA scaffolds. (**A**) Macroscopic image of the 384-well EC-PEGDA scaffolds and 96-well EC-PEGDA scaffolds, scale bar 1 mm; (**B**) SEM of EC-PEGDA scaffold, scale bar 500 µm; (**C**) MicroCT scan of dry EC-PEGDA scaffold, scale bar 1 mm; (**D**) MicroCT scan of dry EC-PEGDA scaffold highlighting porous space, scale bar 1 mm; (**E**) MicroCT scan of dry EC-PEGDA scaffold, scale bar 1 mm; (**F**) MicroCT scan of dry EC-PEGDA scaffold highlighting porous space, scale bar 1 mm.

3.1.5. Rheology

Under stress, a viscoelastic material stores energy like an elastic solid and dissipates energy like a viscous liquid. This response is time-dependent, meaning deformation depends on how fast a force is applied. In contrast, flow characteristics describe how a material's viscosity changes as a result of external forces and temperature. Analysis identified that the EC-PEGDA scaffold showed elastic, solid-like behaviour, evident through the storage modulus (G′) being consistently higher than the loss modulus (G″), with no crossover between G′ and G″, suggesting a stable percolated network structure that resists breakdown under oscillatory deformation (Figure 4A). Typical hydrated 3D models are hydrogels, which exhibit storage moduli in the range of 10^2–10^3 Pa, which is significantly lower than the G′ demonstrated in this material [44].

Complex viscosity (η*) showed shear thinning behaviour, decreasing as angular frequency increased (Figure 4B). This suggests the scaffolds can resist deformation under low-frequency conditions, becoming more deformed under dynamic stress. This is useful, as the scaffold needs to remain stable under static culture conditions while simultaneously accommodating small levels of deformation arising from cellular activity.

Collectively, the mechanical and rheological data demonstrate that the developed EC-PEGDA scaffold has optimal attributes for both production and biological performance. Scaffolds display thermal stability, appropriate integration of eggshell and chitosan, and

favourable mechanical characteristics for replicating trabecular bone. The Young's modulus and compressive strength indicate that the scaffold can sustain load and maintain structural integrity while hydrated, and the rheological analysis across all frequencies confirmed that the material behaves predominantly as a solid, with limited capacity for viscous dissipation. However, the strong elastic dominance and low energy dissipation lead to a degree of brittleness, as the scaffold is less able to redistribute stress before failure. This is consistent with the compressive results and reflects the reinforcement with the eggshell, enhancing stiffness but reducing toughness.

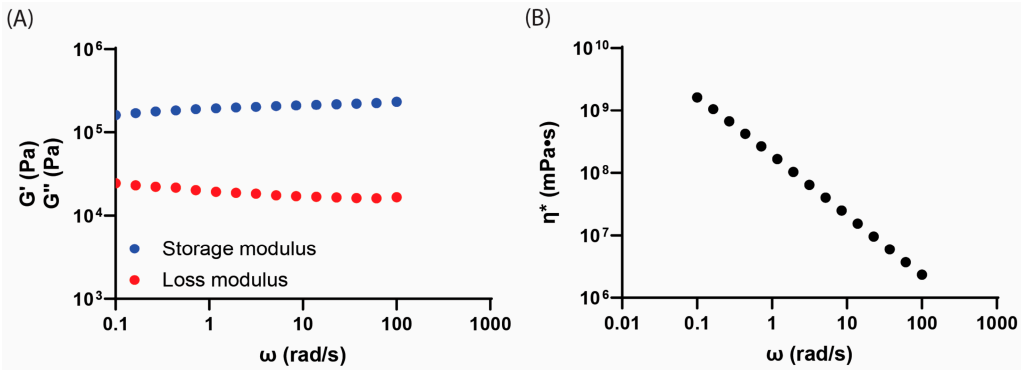


Figure 4. Viscoelastic properties and viscosity of EC-PEGDA scaffolds. (**A**) Storage (G′; blue dots) and loss (G″; red dots) modulus of EC-PEGDA scaffolds ($n = 8$); (**B**) complex viscosity (η*) of EC-PEGDA scaffolds ($n = 8$).

Despite this, the high stiffness, elastic stability and viscoelasticity suggest the scaffold can provide appropriate cues for osteogenic differentiation while maintaining form in vitro. This positions it as a suitable material to be used for in vitro studies recapitulating the bone microenvironment.

3.2. Biological Performance

3.2.1. Visualisation

A key property of an HTS compatible system is imaging capability. Many solid 3D cultures are opaque, limiting in situ imaging. The EC-PEGDA scaffold has demonstrated ability to have cells imaged directly in the scaffold, with the ability to differentiate morphology. Distinct differences in morphology and cytoskeletal arrangement can be seen between the PC-3 cells (Figure 5A) and HS-5 cells (Figure 5B). PC-3 cells formed multicellular spheroids, with irregularly shaped, grape-like loose clusters, while HS-5 cells formed more densely packed, circular spheroids, consistent with morphology in 3D culture [11,12]. Alongside confocal imaging, we were able to successfully image cells attached to scaffolds using SEM, highlighting cellular attachment and spheroid formation (Figure 5C). It is important to note that SEM runs under a vacuum, and as such, the samples need to be dry. Due to the swelling nature of the material, this means that the scaffolds may have shrunk and could potentially have altered the shape of the spheroids.

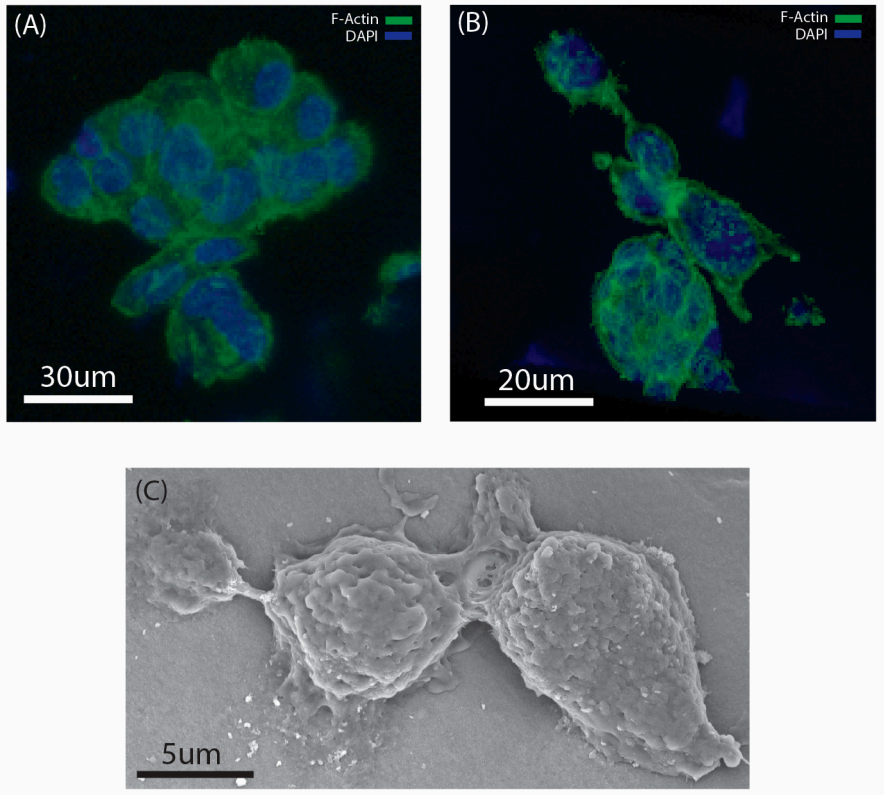


Figure 5. Confocal and SEM imaging of cells showing cellular morphology in EC-PEGDA scaffolds after 7 days in culture. Representative confocal images of (**A**) PC-3 cells and (**B**) HS-5 cells stained with F-Actin (green) and DAPI (blue). (**C**) SEM image of PC-3 cells on scaffold surface after 7 days of culture.

3.2.2. Metabolic Activity

Metabolic activity was assessed in cell lines representative of the metastatic prostate cancer niche, including PC-3, LNCaP, HS-5, hFOB1.19, Hs27 and respective co-culture and reactive lines mentioned in 2.3.2 (Figure 6, Supplementary Figure S1). This was completed to evaluate cytocompatibility of the cell lines with the scaffold. Overall, metabolic activity was reduced in 3D culture compared to 2D across multiple cell types, with significant decreases observed in HS-5 and LNCaP cells. HS-5 cells exhibited metabolic activity of 36.97 ± 9.16 RFU in 3D culture, compared to 101.7 ± 4.49 RFU in 2D culture ($p < 0.0001$). Similarly, LNCaP cells showed reduced metabolic activity in 3D culture, 207.8 ± 1.40 RFU, relative to 2D culture (288.5 ± 25.81 RFU, $p < 0.01$). Remaining cell lines demonstrated a similar trend towards reduced metabolic activity in 3D culture, although this did not meet statistical significance.

The observed reduction in metabolic activity is consistent with the diffusion gradients associated with 3D culture systems, including restricted nutrient transport and waste removal [45]. However, these systems may indicate the establishment of physiologically relevant gradients and cellular heterogeneity that better resemble the in vivo tumour microenvironment. Although cytocompatibility was demonstrated through 72 h viability assessments, this is considered a short-term assay, and longer-term evaluation of cell proliferation, total cell number and viability will be necessary to determine the capacity of the EC-PEGDA scaffold to support sustained cellular growth and remodelling over extended culture periods.

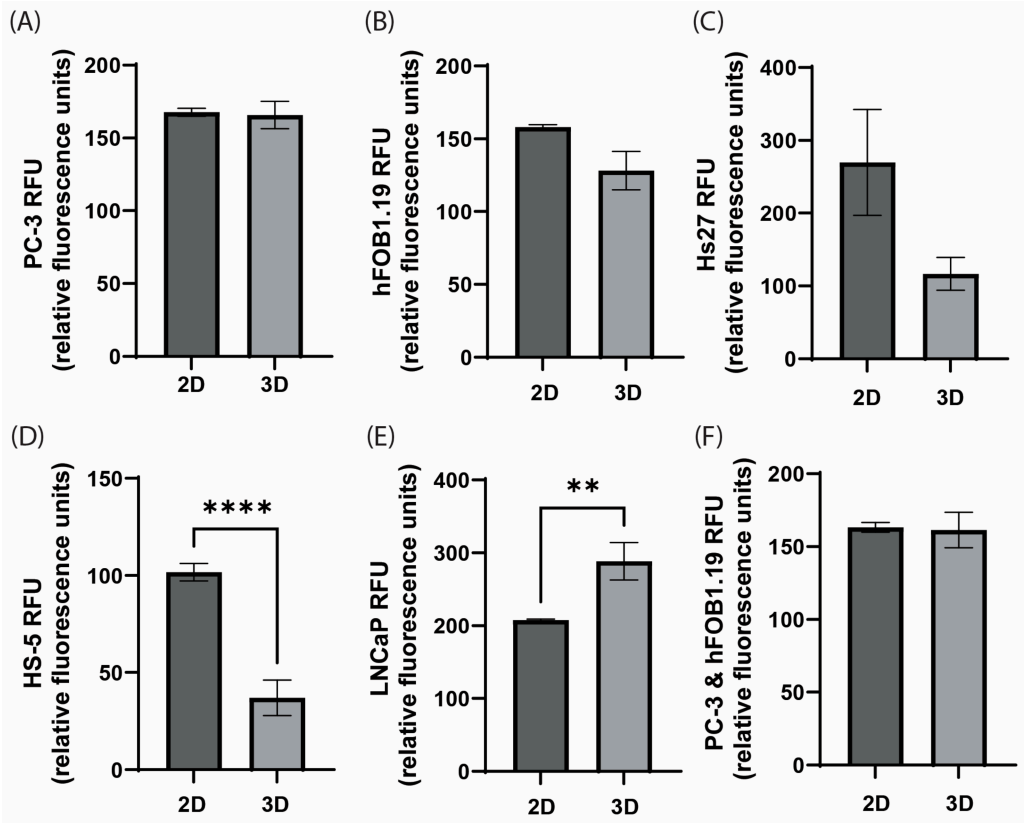


Figure 6. Metabolic activity of monoculture and co-culture on EC-PEGDA scaffolds at 72 h. (**A**) PC-3 cells; (**B**) hFOB1.19 cells; (**C**) Hs-27 cells; (**D**) HS-5 cells; (**E**) LNCaP cells; (**F**) hFOB1.19 and PC-3 co-culture. Data presented as means ± standard error of mean. Significance calculated using a Kruskal–Wallis ANOVA; significance denoted at ** = $p < 0.01$, = **** = $p < 0.0001$.

3.2.3. Osteoblastic Differentiation and Mineralisation

ALP activity was used to evaluate osteoblastic activity. Osteoblastic activity was significantly increased in 3D monoculture compared to 2D monoculture ($p < 0.05$), as indicated by elevated ALP levels (Figure 7A), suggesting enhanced osteoblastic differentiation within the model. This finding is consistent with previous reports showing that physiologically relevant 3D environments promote osteoblastic differentiation and mineralisation [46]. In contrast, co-culture with PC-3 cells resulted in marked suppression of ALP activity in 3D conditions compared to both 2D co-culture and hFOB1.19 monoculture controls ($p < 0.001$, $p < 0.0001$; Figure 7B and 7C, respectively). This reduction in ALP activity suggests that co-culture with PC3 cells disrupts normal bone homeostasis and inhibits osteoblastic differentiation. This is consistent with reports demonstrating that the PC-3 secretome negatively affects osteoblast function [47] and indicates that the model recapitulates key aspects of the dysregulated bone remodelling associated with metastatic prostate cancer.

Extracellular calcium did not differ significantly between 2D and 3D conditions (Figure 7D) or between monoculture and co-culture (Figure 7E). Although ALP activity was substantially reduced in the presence of PC-3 cells, these changes did not translate into detectable differences in extracellular calcium during the study period, suggesting alterations in osteoblast function preceded measurable changes in mineral deposition.

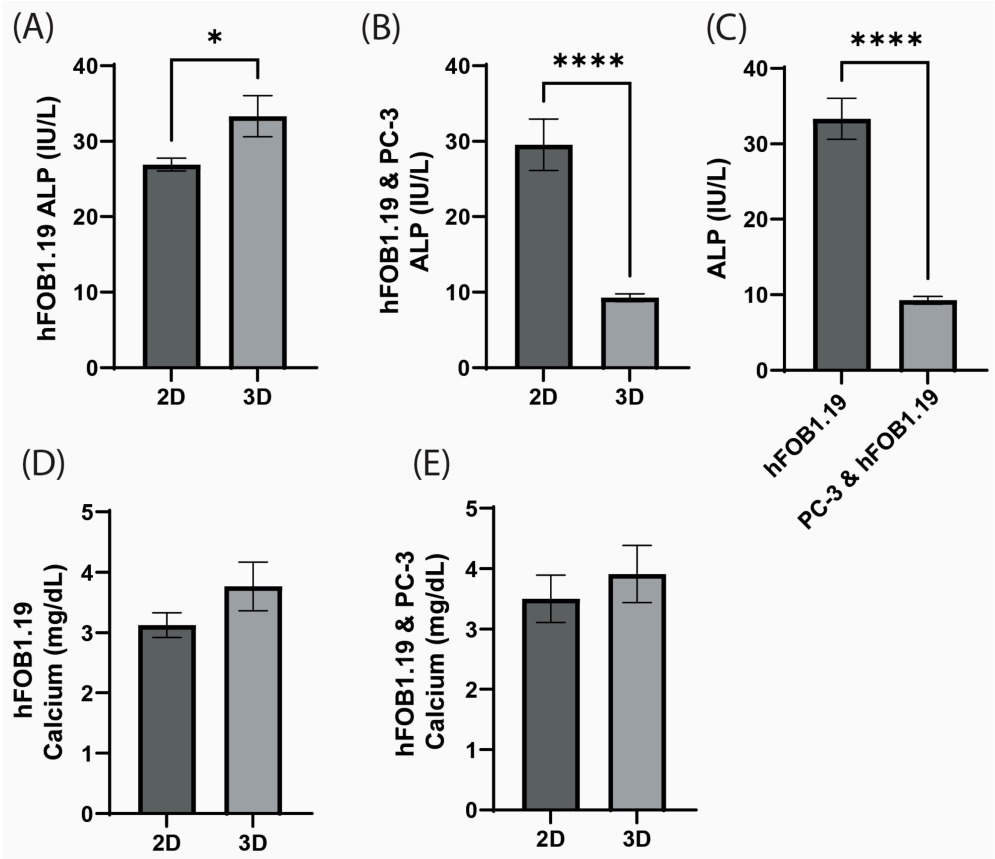


Figure 7. ALP activity in 2D versus EC-PEGDA scaffold-based 3D cultures of (**A**) hFOB1.19 cells and (**B**) hFOB1.19/PC-3 co-cultures; (**C**) ALP activity in 3D hFOB1.19 monocultures versus 3D hFOB1.19/PC-3 co-cultures. Calcium levels in 2D versus 3D cultures of (**D**) hFOB1.19 cells and (**E**) hFOB1.19/PC-3 co-cultures. Data are presented as mean ± SEM. Statistical significance was assessed using Welch's *t*-test: * $p < 0.05$, **** = $p < 0.0001$.

3.2.4. High-Throughput Screening Compatibility

The explicit, quantitative reporting of inter- and intra-plate CV% and Z′ assays is crucial when stating HTS compatibility. Many current solid models that claim HTS or drug discovery compliance fail to quantitatively report these values and rather just state that compliance is appropriate [21,48,49]. It is well known that there is increased variability when using 3D cell culture [50,51] due to inherent interference with the scaffold itself and batch-to-batch variability due to the natural polymers included [52]. Specifically with organ-on-a-chip models, the ability to find Z′ values within historically appropriate levels remains challenging [53]. In vitro 3D cell culture is repeatedly reported as the way forward for drug discovery, with a recent study finding that only 6.9% of drugs from pre-clinical trials pass successfully through clinical trials [54]. The field is largely at an impasse, knowing that 3D cell culture is superior in terms of biological relevance [8,51],while acknowledging the inherent difficulty in eliminating batch–batch variability and that variability across samples is too high to be validated against current standards [55]. This variability is multifactorial, including uneven cellular growth, with spheroids growing in random places and configurations, changes in nutrient diffusion across different areas of the scaffold, and differences in the natural polymers used to create the scaffolds. The majority of 3D cultures that have been validated for HTS use a selection process to obtain similar-sized spheroids or regions of interest (ROI), to ensure results are more reproducible with a CV% of less than 5% [56]. This raises a concern around the generalisability of data. If current drug screening processes rely on selecting individual spheroids that are growing in a similar way,

this may also be selectively testing drugs on cells that have a genetic similarity, not showing the heterogeneity seen across a whole organism. Our current model does not yet meet the robust requirements for HTS screening (Table 4); however, the scaffold demonstrates compatibility with imaging-based high-throughput workflows. Additionally, use of an ROI opposed to global assessment of cellular activity would likely improve reproducibility.

Table 4. Assessment of high-throughput screening (HTS) compatibility in 2D and EC-PEGDA scaffold-based 3D cultures. Inter-plate and intra-plate coefficients of variation (CV%) indicate assay variability, while the Z′ factor measures assay quality based on the separation and variability of positive and negative controls.

	Inter-Plate CV%	Intra-Plate CV%	Z′
2D	14.54	8.66	0.7049
3D	35.09	30.72	−0.5459

The EC-PEGDA platform therefore represents an important intermediate step towards image-based screening applications. Future work will focus on reducing assay variability, refining experimental workflows and establishing the performance metrics required for high-throughput drug discovery screening environments.

3.2.5. Cytokine Analysis

Two-Dimensional Versus Three-Dimensional Monoculture Activates Cytokine Networks

The 3D culture induced a substantial increase in cytokine signalling compared to 2D culture conditions, with elevated expression of interleukin (IL)-6, granulocyte macrophage colony stimulating factor (GM-CSF), and IL-18 and IL-1 family cytokines (Figure 8). Several cytokines, including interferon gamma (IFN-γ), IL-2 and IL-15, were detected exclusively in 3D culture. This indicates that the 3D scaffold environment enables activation of signalling networks that are largely absent in monolayer systems, consistent with enhanced cell–matrix interactions and spatial organisation.

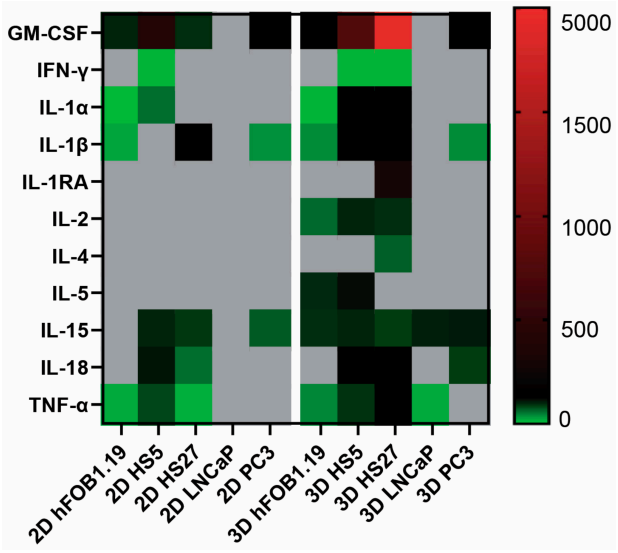


Figure 8. Heatmap of cytokine release in 2D and 3D cell culture systems on EC-PEGDA scaffolds after 72 h of culture. Heatmap showing cytokine concentrations in culture supernatants from hFOB1.19, HS-5, Hs27, LNCaP and PC-3 cells. Rows represent individual cytokines, and columns represent cell lines under each culture condition. Colours indicate increasing concentrations from green through black to red, and grey indicates no detectable cytokines.

Contact-Mediated Versus Soluble-Mediated Mechanisms of Signalling

Cytokine profiles differed substantially between contact-mediated co-culture and conditioned media experiments (Figure 9A). Notably, soluble factor-mediated conditions consistently induced higher cytokine expression across multiple targets (Figure 9B). Of the 25 cytokines tested, GM-CSF, IL-10, IFN-γ, IL-1α, IL-1β, IL-1RA, IL-2, IL-4, IL-5, IL-15, IL-18, and tumour necrosis factor alpha (TNF-α) showed measurable levels in both co-culture and soluble factor-mediated culture. IL-6 concentrations exceeded the upper limit of quantification of the multiplex assay and therefore could not be reliably quantified. These findings suggest that soluble-factor-mediated signalling contributes substantially to the increased net cytokine concentrations observed in culture supernatants.

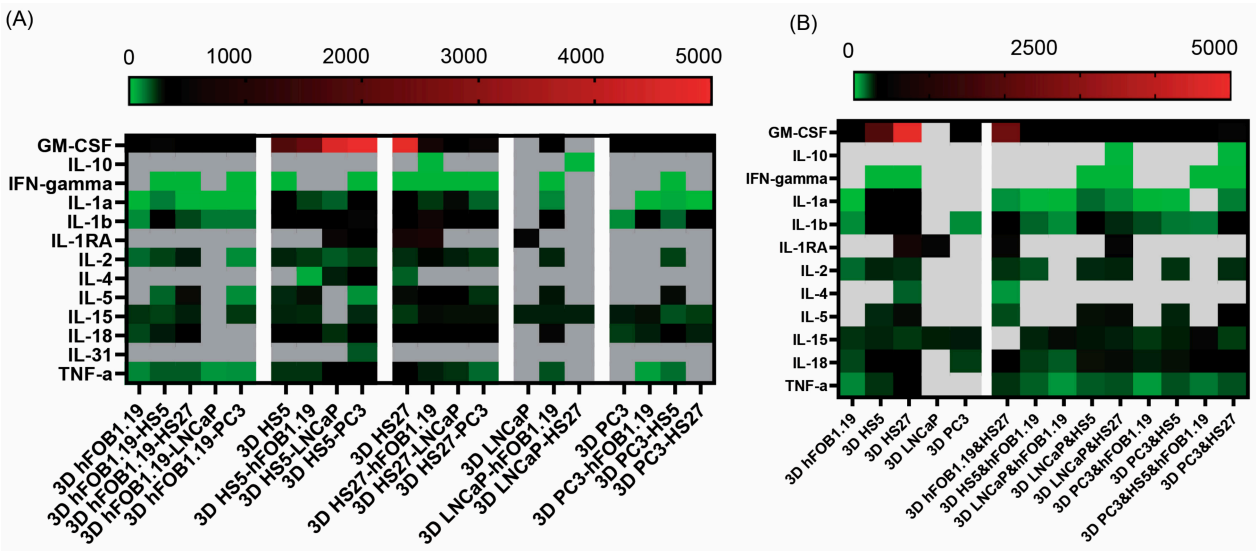


Figure 9. Cytokine profiles following conditioned-medium exposure and direct co-culture in EC-PEGDA scaffolds after 72 h. Heatmaps showing cytokine concentrations in culture supernatants from (**A**) soluble-mediated cytokine release after 72 hand (**B**) contact-mediated cytokine release after 72 h. Rows represent individual cytokines, and columns represent the indicated culture conditions. In panel (**A**), the recipient cell line is listed first, followed by the conditioned-medium donor cell line. Colours indicate increasing concentrations from green through black to red, and grey indicates no detectable cytokines.

Importantly, IL-6 consistently exceeded the upper limit of the assay reference range, preventing accurate quantitative comparisons between experimental groups. Although this precludes conclusions regarding relative differences between conditions, the repeated detection of IL-6 above the assay range indicates substantial IL-6 secretion within the model and is therefore biologically noteworthy. Given the established involvement of IL-6 signalling in prostate cancer progression, stromal activation and bone remodelling, this finding suggests that the EC-PEGDA system supports cytokine networks relevant to the metastatic bone niche.

However, the magnitude and condition-specificity of this response cannot be determined from the present dataset. The multiplex nature of the assay and relatively low abundance of other cytokines meant sample dilution was not feasible. Overall, there was a marked increase in cytokine release in soluble culture, likely due to the bidirectional nature of co-culture, where cytokine release can be altered; also, uptake of cytokines can reduce the levels detected in media. Due to cytokine release profiles and reported clinical relevance in prostate cancer progression and bone metastasis, GM-CSF, IL-1α, IL-1β, IL-2 and TNF-α were used for downstream analysis [57,58].

The development of a pre-metastatic niche relies on secondary site cells reacting to circulating cytokines released by the primary tumour. To model this process, HS-5 stromal cells were exposed to tumour-conditioned media, allowing the effects of soluble tumour-secreted factors to be assessed independently of direct cell–cell interactions. Overall, conditioned media included stronger cytokine responses than co-culture conditions, suggesting that tumour-secreted factors are sufficient to activate stromal cells and initiate inflammatory signalling. HS-5 cells treated with PC-3-conditioned media induced significantly higher expression of proinflammatory cytokines, including GM-CSF ($p < 0.0001$; Figure 10A), IL-1α ($p < 0.0001$; Figure 10B), IL-1β ($p < 0.0001$; Figure 10C) and TNF-α ($p < 0.001$; Figure 10D) compared to PC-3 and HS-5 co-culture. In comparison, HS-5-LNCaP showed a significant increase in only GM-CSF ($p = 0.0338$; Figure 10A). The differential cytokine responses observed between PC-3 and LNCaP conditions may reflect their distinct biological phenotypes, with PC-3 cells representing a more aggressive inflammatory tumour state, while LNCaP cells retain features of hormone-sensitive disease.

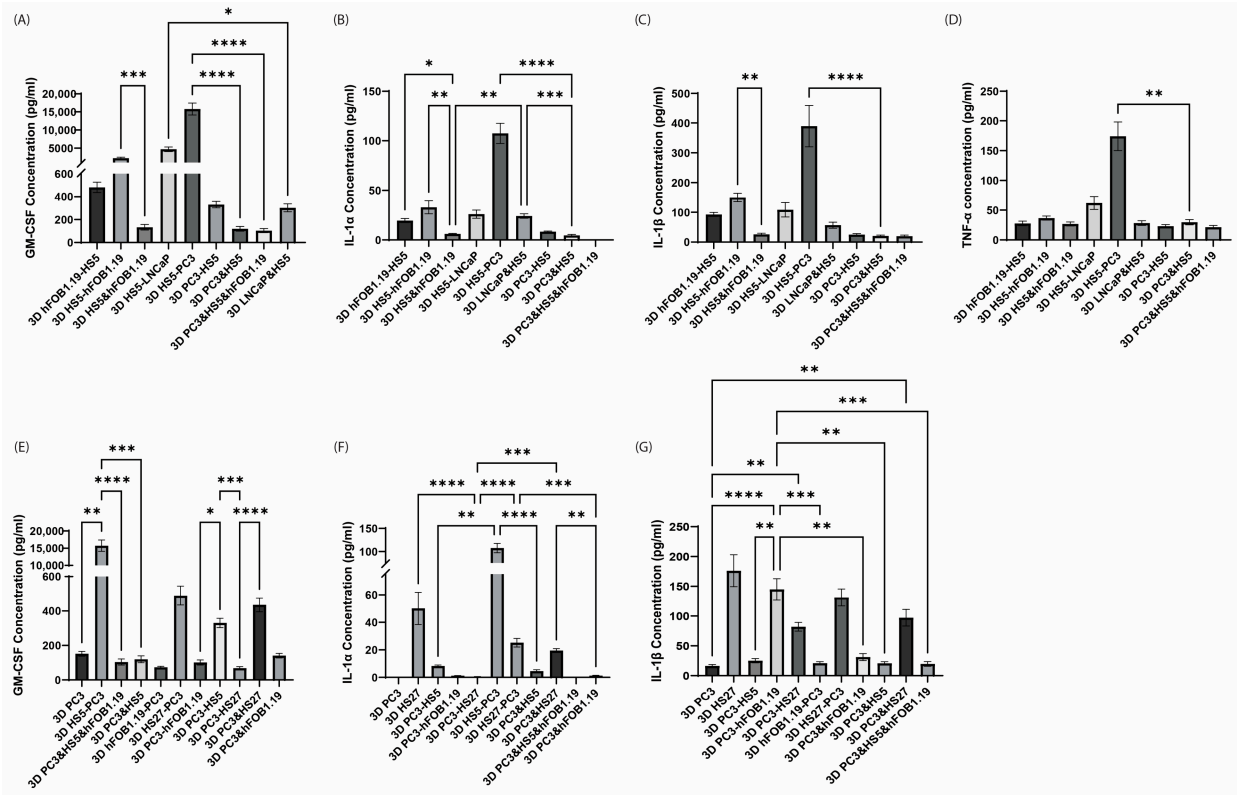


Figure 10. Quantitative analysis of key cytokines associated with tumour–stroma signalling. (**A**,**E**) GM-CSF; (**B**,**F**) IL-1α; (**C**,**G**) IL-1β; (**D**) TNF-α. Cytokine expression was compared across conditioned media and co-culture conditions for tumour (PC-3, LNCaP), stromal (HS-5) and control (Hs27, hFOB1.19) cell lines. Data presented as mean ± SEM. Statistical significance determined using a Kruskal–Wallis ANOVA, with Dunn's post hoc. Significance denoted as * = $p < 0.05$, ** = $p < 0.01$, *** = $p < 0.001$, = **** $p < 0.0001$.

The additional induction of IL-1α, IL-1β and TNF-α by PC-3-conditioned media may reflect inflammatory pathways associated with a more advanced and bone tropic phenotype. To confirm this was not an artifact of general stromal activation, Hs27 cells were utilised as a control, and no differences were found in co-culture compared to soluble factors (Figure 10D). This suggests that soluble factors released from primary site tumours may be sufficient to drive initial stromal activation in the absence of cell–cell contact, while also being site-specific. GM-CSF may be an initial precursor to the priming of the metastatic niche. Chronic GM-CSF exposure has been implicated in the recruitment and expansion of

the immunosuppressive myeloid population, including myeloid-derived suppressor cells and immunosuppressive macrophages [59]. This aligns with pre-metastatic niche models, whereby primary tumours secrete soluble mediators capable of remotely reprogramming distant tissues prior to tumour cell colonisation.

We also assessed the effect of hFOB 1.19-conditioned media on HS-5 and Hs27 cells. HS-5-hFOB1.19 showed significantly higher cytokine levels than HS-5 and hFOB1.19 in GM-CSF ($p = 0.0003$; Figure 10A), IL-1α ($p = 0.0023$; Figure 10B) and IL-1β ($p = 0.0012$; Figure 10C), while no differences were found with Hs27 cells (Figure 10E–G). As HS-5 and hFOB1.19 cells are representative of the normal microenvironment, this suggests that cytokine signalling is part of the normal stromal osteoblastic communication. Bone is highly dynamic and undergoes continuous remodelling, with cytokines and growth factors contributing to the regulation of bone turnover, and cellular communication and tissue repair [60] to bone turnover, haematopoiesis and tissue repair. Consequently, the observed cytokine increases may reflect more physiological signalling as opposed to tumour activation.

Cytokine Profiles Associated with Tumour–Stroma Communication

To determine whether the observed cytokine changes extended beyond baseline stromal–osteoblastic communication, cytokine profiles were compared across tumour-, stromal- and osteoblast-associated conditions. Stromal responses to tumour-derived signals were markedly dependent on tumour type, with PC-3-associated conditions producing a more pronounced inflammatory response than either LNCaP or osteoblastic controls.

Within HS-5 stromal cells, exposure to PC-3-conditioned media resulted in significant upregulation of multiple pro-inflammatory cytokines. GM-CSF expression in HS-5-PC-3 cells was significantly higher than HS-5 cells alone ($p < 0.0001$), HS-5-hFOB1.19 cells, ($p < 0.0001$) and HS-5-LNCaP cells ($p < 0.05$; Figure 11A); Similarly, IL-1β expression was significantly higher in HS-5-PC-3 cells compared to HS-5 cells alone ($p < 0.05$), HS-5-hFOB1.19 cells ($p < 0.05$) and HS-5-LNCaP cells ($p < 0.001$; Figure 11C), while TNF-α expression was significantly higher than HS-5 cells alone ($p < 0.0001$), HS-5-hFOB1.19 cells ($p < 0.0001$) and HS-5-LNCaP cells ($p < 0.05$; Figure 11D). Although IL-1α showed significant increase compared to HS-5-hFOB1.19 cells ($p < 0.0001$) and HS-5-LNCaP cells ($p < 0.0001$), no difference was observed between HS-5 cells alone and HS-5-PC-3 cells (Figure 11B). This suggests that IL-1α is associated with intrinsic stromal signalling. Interestingly, HS-5 cells alone showed significantly higher expression of IL-1α compared to HS-5-LNCaP cells ($p < 0.05$). Collectively, these findings indicate that PC-3-derived factors selectively amplify cytokine signalling within HS-5-containing cultures. The elevated expression of GM-CSF, IL-1β and TNF-α demonstrates a distinct cytokine profile relative to osteoblastic and LNCaP-associated conditions and is consistent with inflammatory signalling processes associated with prostate cancer progression within bone.

Analysis of PC-3-centred interactions further supported a role for stromal activation in establishing a pro-metastatic microenvironment. GM-CSF expression in PC-3-HS-5 cells was significantly higher than PC-3-hFOB1.19 cells ($p < 0.0001$) and PC-3-LNCaP cells ($p < 0.0001$), while there was no change compared to PC-3 cells alone (Figure 11E); however, GM-CSF expression in PC-3-Hs27 cells was significantly lower than PC-3 cells alone ($p < 0.05$; Figure 11E). IL-1α was not detected in monoculture; however, in the presence of conditioned media, PC-3-HS-5 cells showed a significant increase compared to PC-3-hFOB1.19 cells ($p < 0.01$) and PC-3-Hs27 cells ($p < 0.0001$; Figure 11F). IL-1β expression was significantly higher in PC-3-HS-5 cells than HS-5 cells alone ($p < 0.0001$) and PC-3-HS-5 cells ($p < 0.0001$). Compared to PC-3-Hs27 cells, PC-3-HS-5 cells had lower IL-1β expression ($p < 0.05$), as did PC-3 cells alone ($p < 0.001$; Figure 11G). These findings suggest that interactions between aggressive tumour cells and bone marrow stromal cells generate a

distinct inflammatory profile that is not reproduced by osteoblastic or tumour-derived interactions alone.

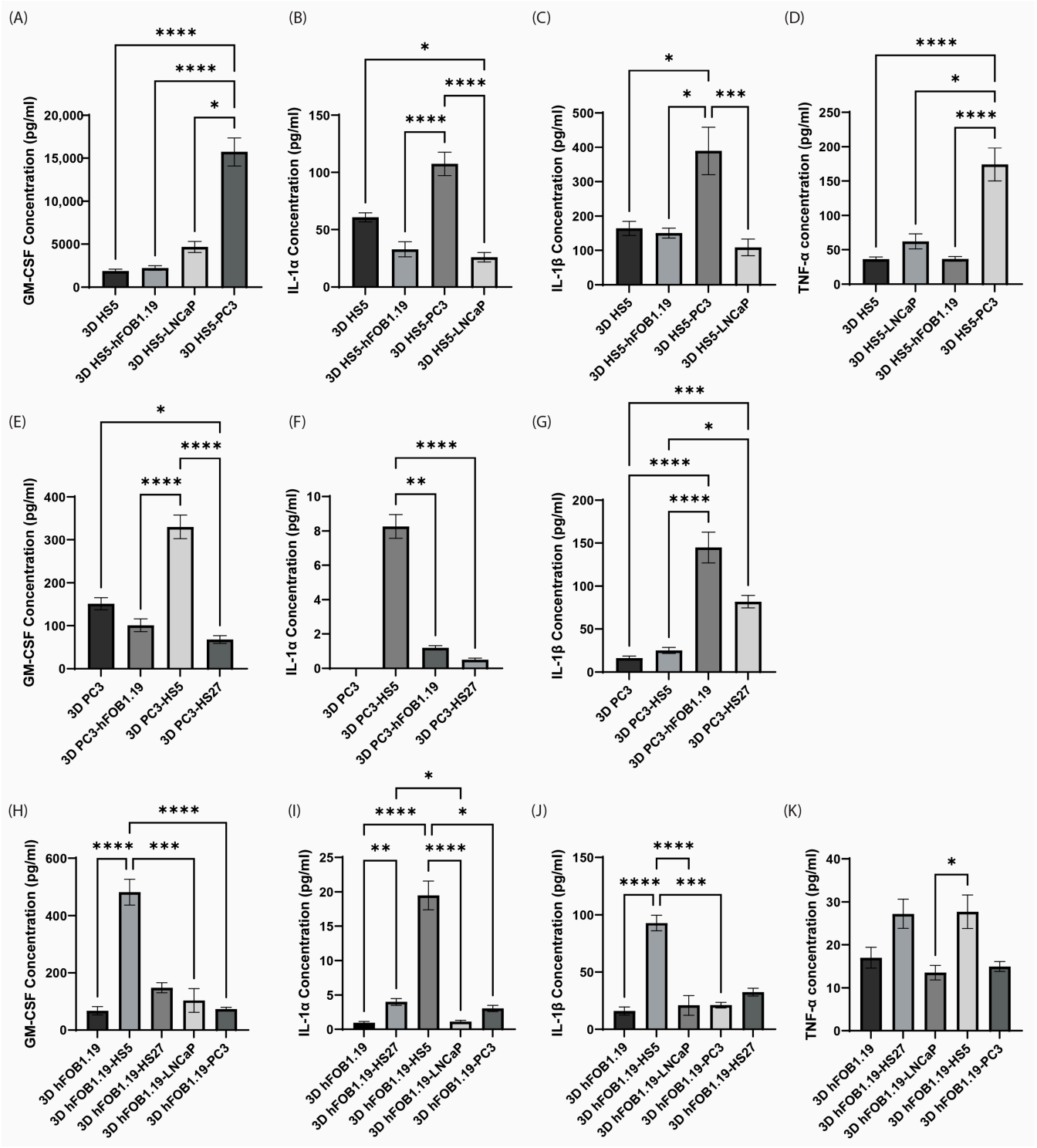


Figure 11. Cytokine profiling across tumour, stromal and osteoblastic conditions to assess tumour–stroma inflammatory signalling within a bone-mimetic microenvironment. Expression of key cytokines (GM-CSF, IL-1α, IL-1β, TNF-α) was evaluated across monoculture, co-culture and conditioned media conditions for (**A**–**D**) HS-5, (**E**–**G**) PC-3 and (**H**–**K**) hFOB1.19 cells. Data presented as mean ± SEM. Statistical significance determined using Kruskal–Wallis test with Dunn's post hoc analysis, with comparisons made between relevant biological groups. Significance denoted as * = $p < 0.05$, ** = $p < 0.01$, *** = $p < 0.001$, **** = $p < 0.0001$.

In contrast, hFOB1.19 cells demonstrated a cytokine profile more consistent with normal cellular communication, with cytokine expression being influenced primarily by interactions with stromal cells rather than tumour cells. GM-CSF expression was significantly higher in hFOB1.19-HS-5 cells than hFOB1.19s cells alone ($p < 0.0001$), hFOB1.19-PC-3 cells ($p < 0.0001$) and hFOB1.19-LNCaP cells ($p < 0.0001$; Figure 11H). Similarly, IL-1α expression was elevated in hFOB1.19-HS-5 cells relative to hFOB1.19s cells alone ($p < 0.0001$), hFOB1.19-LNCaP cells ($p < 0.0001$) and hFOB1.19-PC-3 cells ($p < 0.05$; Figure 11I). IL-1α expression in hFOB1.19-Hs27 cells was significantly higher than hFOB1.19 cells alone ($p < 0.01$) and hFOB1.19-LNCaP cells ($p < 0.05$; Figure 11I), further supporting a role for stromal–osteoblastic interactions in regulating basal cytokine signalling.

A similar pattern was observed for IL-1β, with expression significantly higher in hFOB1.19-HS-5 cells compared to hFOB1.19 cells alone ($p < 0.0001$), hFOB1.19-LNCaP cells ($p < 0.0001$) and hFOB1.19-PC-3 cells ($p < 0.0001$; Figure 11J). No differences in IL-1β expression were detected between hFOB1.19 cells alone and co-culture with anything other than HS-5, suggesting it is not a driver of the metastatic microenvironment and instead is part of normal cell signalling.

TNF-α showed minimal variation across conditions, with the only significant difference being higher expression in hFOB1.19-HS-5 cells compared to hFOB1.19-LNCaP cells ($p < 0.05$; Figure 11K). Collectively, these findings indicate that cytokine changes in hFOB1.19 cells are predominantly driven by interactions with stromal ells and do not display the amplified inflammatory profile observed in PC-3-associated conditions. This suggests that elevated GM-CSF, IL-1β and TNF-α signalling identified within PC-3-associated stromal interactions represents a distinct inflammatory profile compared with normal stromal–osteoblastic communication.

Taken together, these results indicate that the cytokine changes associated with PC-3 stromal interactions are distinct from normal stromal–osteoblastic communication. The selective elevation of GM-CSF, IL-1β, and TNF-α within PC-3-associated conditions is consistent with signalling pathways that have been implicated in prostate cancer bone metastasis and metastatic niche development.

Translational Relevance

This study demonstrates that the EC-PEGDA scaffold supports tumour–stroma communication within a structurally relevant bone-mimetic microenvironment. Exposure of HS-5-containing cultures to PC-3-conditioned media was associated with increased concentrations of GM-CSF, IL-1β and TNF-α, while IL-6 consistently exceeded the assay quantification range. Importantly, these cytokines have been implicated in prostate cancer progression, bone remodelling and metastatic disease (Table 5), providing translational context for the signalling profile observed within the EC-PEGDA model. While the cellular origins of these cytokines cannot be determined from bulk supernatant measurements, the findings indicate activation of inflammatory signalling networks relevant to tumour–stroma interactions within bone.

Table 5. Translational relevance of cytokine signalling identified in the EC-PEGDA model.

Cytokine	Finding in EC-PEGDA Model	Reported Relevance to Prostate Cancer/ Bone Metastasis	References
IL-1β	Increased, particularly in PC-3-associated stromal conditions	Associated with aggressive and AR-negative prostate cancer phenotypes, with IL-1β signalling implicated in progression toward AR-independent disease and the bone metastatic microenvironment.	[61–64]

Table 5. *Cont.*

Cytokine	Finding in EC-PEGDA Model	Reported Relevance to Prostate Cancer/ Bone Metastasis	References
GM-CSF	Increased in HS-5 following PC-3-conditioned media	Implicated in tumour-associated myeloid regulation, immunosuppressive signalling and processes contributing to metastatic niche development and bone metastasis.	[59,65–67]
TNF-α	Increased in PC-3-associated stromal conditions	Elevated circulating TNF-α has been reported in metastatic compared with localised prostate cancer and was associated with greater disease extent and progression	[57,58,68]
IL-6	Exceeded assay quantification range	Elevated circulating IL-6 has been reported in metastatic prostate cancer. Importantly for this model, serum IL-6 was significantly higher in prostate cancer patients with bone metastases than those without bone metastases and was related to the extent of osseous metastatic burden.	[57,58,67,69]

IL-1β is implicated in androgen receptor (AR) absence. It has long been known that prostate cancer can progress to androgen independence, and this is characteristic of advanced stage cancers. We identified that IL-1β was expressed by PC-3 cells but not LNCaP cells, which supports the literature that found that AR negative (AR-) prostate cancers have increased expression of IL-1β [61,62], and found that when evaluating human specimens, there was a heterogenous mixture of AR positive (AR+) and AR − cells within the bone metastatic niche, yet the AR − cells were the only ones secreting IL-1β [61]. Chronic exposure to IL-1β can result in AR+ cells becoming AR-independent [63]. Furthermore, it has been demonstrated that the high level of IL-1 secreted by the bone stromal cells can cause AR+ cells to mimic an AR − phenotype, which favours androgen deprivation therapy (ADT) resistance and disease progression [64]. In our study, HS-5-conditioned media resulted in cell death of LNCaP cells, making any cytokine analysis non-feasible; this response has also been identified by other groups [70].

GM-CSF has also been identified as a significant cytokine in the development of bone metastases in prostate cancer and is known to have a multifaceted role, having both pro-, and anti-tumourigenic properties [65]. It promotes the activation of osteoclast precursors and regulates the maturation, recruitment and function of macrophages, neutrophils and other myeloid cell populations [66]. Within the tumour microenvironment, GM-CSF has been implicated in the establishment of immunosuppressive conditions through differentiation and expansion of myeloid-derived suppressor cells (MDSCs). This process is mediated through activation of the JAK2/STAT5 and P13K/AKT signalling pathways [66], which promote development of immunosuppressive myeloid populations and inhibit effective anti-tumour responses. Of note, GM-CSF has also been implicated in post-translational modifications of IL-6 in prostate cancer cells, a potential contributor to disease progression [67]. The elevated GM-CSF levels observed in HS-5-PC-3 cultures are particularly noteworthy given the established role of this cytokine in bone metastasis.

IL-1α, IL-1β and TNF-α are strongly associated with bone metastasis promoting osteoclastogenesis through an increase in RANKL signalling and contribute to tumour-associated bone remodelling. The elevated cytokine signalling observed in HS-5-PC-3 cultures may therefore reflect inflammatory signalling processes relevant to tumour progression and tumour–bone communication.

While not compared statistically due to high expression levels, IL-6 is a downstream target of both the IL-1 family and TNF-α, further contributing to osteoclast differentiation and tumour progression through activation of the STAT3 pathway.

These findings support a model in which tumour-derived factors initiate stromal activation through cytokine secretion, leading to amplification of inflammatory signalling pathways involving GM-CSF, IL-1β and TNF-α. The emergence of cytokine networks exclusively in 3D culture highlights the importance of spatial organisation and cell–matrix interactions in regulating signalling behaviour. Unlike conventional 2D systems, the EC-PEGDA scaffold supports inflammatory signalling pathways that have been implicated in immunomodulation, bone remodelling and processes associated with metastatic niche formation, providing a more physiologically relevant model of prostate cancer bone metastasis.

3.2.6. Limitations

Several limitations should be considered. While variability in 3D culture remains a challenge for traditional HTS metrics, the enhanced biological fidelity observed here highlights a trade-off between reproducibility and physiological relevance. Notably, the compatibility of this scaffold with imaging-based workflows suggests an alternative path forward, where phenotypic screening can be prioritised over bulk readouts.

The use of naturally derived eggshell introduces inherent variability due to biological differences in source material. Here, eggshells were obtained from a large pool of commercially available eggs, contributing to batch-to-batch variation [71–73]. While this may reduce reproducibility relative to synthetic materials, it reflects the heterogeneity expected in sustainable biomaterials and biological systems. Despite this, the scaffold remained compatible with imaging-based workflows, indicating functional robustness despite this variability.

A further limitation is the use of established cell lines rather than patient-derived tumour or stromal cells. Although established cell lines provide greater experimental reproducibility and facilitate systematic characterisation of the scaffold, they do not reproduce the inter-patient heterogeneity or patient-specific tumour phenotypes captured by patient-derived models. The EC-PEGDA scaffold is therefore intended as an intermediate experimental platform rather than a replacement for patient-derived organoid systems. Future incorporation of primary or patient-derived cells alongside immune cells would provide an important step toward assessing whether the signalling behaviours observed here are conserved across clinically heterogeneous prostate cancer samples.

The model also does not currently incorporate an osteoclast component. This is particularly relevant given the observed increases in cytokines associated with regulation of osteoclast differentiation and activity, including IL-1 family cytokines, TNF-α, and GM-CSF. Consequently, although the cytokine profile indicates the activation of pathways capable of influencing bone remodelling, the present study cannot determine the functional effects of this signalling on osteoclastogenesis or bone resorption. Incorporation of osteoclast precursors or differentiated osteoclasts in future studies would enable direct investigation of tumour–stroma–osteoblast–osteoclast interactions and provide a more complete representation of the metastatic bone-remodelling cycle.

As cytokine concentrations were measured in bulk supernatants, the cellular source of the individual cytokines cannot be assigned. Consequently, observed cytokine profiles represent net system-level responses rather than direct evidence of secretion by a specific cell population.

4. Conclusions

Taken together, this study demonstrates that the EC-PEGDA scaffold provides a structurally relevant, imaging-compatible bone-mimetic microenvironment capable of supporting multicellular tumour–stroma culture and assessment of cytokine signalling. The model maintained viability of prostate cancer, stromal and osteoblastic cell populations while supporting biological responses associated with tumour–microenvironment communication.

In particular, exposure to PC-3-derived conditioned medium was associated with altered osteoblastic activity and increased concentrations of GM-CSF, IL-1β and TNF-α within HS-5-containing cultures, indicating activation of cytokine signalling networks relevant to tumour–stroma interactions within bone. Importantly, these findings are consistent with inflammatory processes implicated in prostate cancer progression and bone remodelling.

While cytokine responses were quantified from bulk culture supernatants and therefore could not be assigned to specific cellular populations, the observed signalling changes demonstrate that the EC-PEGDA platform captures biologically relevant communication between tumour-associated and bone-associated cell types. Together with its structural properties, cytocompatibility and compatibility with imaging-based multiwell workflows, the EC-PEGDA scaffold provides a controllable and experimentally accessible platform for investigating tumour–stroma interactions within a bone-relevant environment.

Rather than reproducing the patient-specific complexity of organoid systems, the EC-PEGDA model represents an intermediate platform between conventional in vitro culture and more complex tissue-engineered systems, combining biological relevance with reproducibility, structural stability and imaging accessibility. These characteristics provide a foundation for future studies investigating tumour–microenvironment interactions and for optimisation toward automated imaging-based phenotypic screening workflows.

Future studies incorporating patient-derived cells, osteoclast populations, and higher-resolution approaches such as spatial transcriptomics, proteomics or cell-specific analyses will be required to determine the cellular origins of the observed cytokine responses and establish their relevance to metastatic bone disease. Quantitative validation of highly expressed cytokines, particularly IL-6, will also be important to define the magnitude and condition-specificity of these responses. Finally, alternative manufacturing approaches such as 3D bioprinting could be explored to provide greater architectural control and tunability. Together, these developments may further establish the EC-PEGDA scaffold as a biologically relevant and scalable platform for modelling aspects of prostate cancer–bone microenvironment interactions and evaluating therapeutic responses.

Supplementary Materials: The following supporting information can be downloaded at: https://www.mdpi.com/article/10.3390/biomimetics11110836/s1, Figure S1: Metabolic activity of 2D compared to 3D cultures at 72 h.

Author Contributions: Conceptualization, L.C.E.W. and A.R.; methodology, A.R., J.F. (Jarred Facer), D.M.S., D.A., J.F. (Jessica Feldman), E.W., P.B. and L.C.E.W.; formal analysis, A.R., D.M.S., J.F. (Jarred Facer) and D.A.; investigation, A.R., J.F. (Jarred Facer), D.M.S., D.A., J.F. (Jessica Feldman) and L.C.E.W.; resources, L.C.E.W. and C.W.; data curation, A.R.; writing—original draft preparation, A.R.; writing—review and editing, L.C.E.W., N.W., P.B., J.F. (Jessica Feldman), J.F. (Jarred Facer), D.M.S., D.A., E.W. and C.W.; visualization, A.R. and L.C.E.W.; supervision, L.C.E.W., N.W., P.B., E.W., J.F. (Jessica Feldman) and C.W.; project administration, A.R. and L.C.E.W.; funding acquisition, P.B. and L.C.E.W. All authors have read and agreed to the published version of the manuscript.

Funding: This work was funded by the Australian Government Department of Education through a Regional Research Collaboration (RRC) grant. This funding allowed the establishment of the University of Southern Queensland-led SIMPLE Hub, where this research was conducted. Additionally, this research was supported by the Australian Government Research Training Program Scholarship.

Institutional Review Board Statement: This study received Ethics committee approval from the University of Southern Queensland Human Research Ethics Committee (ETH2023-0263).

Data Availability Statement: Data are available on request.

Acknowledgments: The authors would like to acknowledge the Microscopy and Spatial Cell Biology Facility, Scientific Services QIMR Berghofer, and the Lions Club of Australia and the Mater Foundation for funding the Skyscan 1272, and the Preclinical Imaging Facility at TRI for providing resources

that enabled this research. The authors would also like to acknowledge the University of Southern Queensland teaching technical staff for facilitating the use of equipment required for this study, Anna Singleton for photography, and the technical staff that maintain the Centre for Future Materials laboratories for their technical assistance throughout. The graphical abstract was created using BioRender. Created in BioRender. Reinke, A. (2026) https://BioRender.com/i69n3zh.

Conflicts of Interest: The authors declare no conflicts of interest.

References

1. Harrison, R.K. Phase II and phase III failures: 2013–2015. *Nat. Rev. Drug Discov.* **2016**, *15*, 817–818. [CrossRef] [PubMed]
2. Sun, D.; Gao, W.; Hu, H.; Zhou, S. Why 90% of clinical drug development fails and how to improve it? *Acta Pharm. Sin. B* **2022**, *12*, 3049–3062. [CrossRef] [PubMed]
3. Bowling, H.; Cocucci, A.; Koo, D.C.E.; Harrison, R.K. Analysis of phase II and phase III clinical trial terminations from 2013 to 2023. *Nat. Rev. Drug Discov.* **2025**, *25*, 5. [CrossRef] [PubMed]
4. Fernald, K.D.S.; Förster, P.C.; Claassen, E.; van de Burgwal, L.H.M. The pharmaceutical productivity gap–Incremental decline in R&D efficiency despite transient improvements. *Drug Discov. Today* **2024**, *29*, 104160. [CrossRef] [PubMed]
5. Sundberg, S.A. High-throughput and ultra-high-throughput screening: Solution- and cell-based approaches. *Curr. Opin. Biotechnol.* **2000**, *11*, 47–53. [CrossRef] [PubMed]
6. Denyer, J.; Worley, J.; Cox, B.; Allenby, G.; Martyn, B. HTS approaches to voltage-gated ion channel drug discovery. *Drug Discov. Today* **1998**, *3*, 323–332. [CrossRef]
7. Garnique, A.; Parducci, N.S.; de Miranda, L.B.L.; de Almeida, B.O.; Sanches, L.; Machado-Neto, J.A. Two-Dimensional and Spheroid-Based Three-Dimensional Cell Culture Systems: Implications for Drug Discovery in Cancer. *Drugs Drug Candidates* **2024**, *3*, 391–409. [CrossRef]
8. Windus, L.C.E.; Kiss, D.L.; Glover, T.; Avery, V.M. In vivo biomarker expression patterns are preserved in 3D cultures of Prostate Cancer. *Exp. Cell Res.* **2012**, *318*, 2507–2519. [CrossRef] [PubMed]
9. Karkampouna, S.; La Manna, F.; Benjak, A.; Kiener, M.; De Menna, M.; Zoni, E.; Grosjean, J.; Klima, I.; Garofoli, A.; Bolis, M.; et al. Patient-derived xenografts and organoids model therapy response in prostate cancer. *Nat. Commun.* **2021**, *12*, 1117. [CrossRef] [PubMed]
10. Wang, H.-M.; Zhang, C.-Y.; Peng, K.-C.; Chen, Z.-X.; Su, J.-W.; Li, Y.-F.; Li, W.-F.; Gao, Q.-Y.; Zhang, S.-L.; Chen, Y.-Q.; et al. Using patient-derived organoids to predict locally advanced or metastatic lung cancer tumor response: A real-world study. *Cell Rep. Med.* **2023**, *4*, 100911. [CrossRef] [PubMed]
11. Windus, L.C.E.; Glover, T.T.; Avery, V.M. Bone-stromal cells up-regulate tumourigenic markers in a tumour-stromal 3D model of prostate cancer. *Mol. Cancer* **2013**, *12*, 112. [CrossRef] [PubMed]
12. Windus, L.C.E.; Matigian, N.; Avery, V.M. Induction of Reactive Bone Stromal Fibroblasts in 3D Models of Prostate Cancer Bone Metastases. *Biology* **2023**, *12*, 861. [CrossRef] [PubMed]
13. Sato, T.; Vries, R.G.; Snippert, H.J.; van de Wetering, M.; Barker, N.; Stange, D.E.; Van Es, J.H.; Abo, A.; Kujala, P.; Peters, P.J.; et al. Single Lgr5 stem cells build crypt-villus structures in vitro without a mesenchymal niche. *Nature* **2009**, *459*, 262–265. [CrossRef] [PubMed]
14. Reinke, A.; Ward, G.; Feldman, J.; Whiteside, E.J.; Paulomi, B.; Windus, L.C.E. Bioengineered in vitro bone scaffolds to investigate bone metastases: A systematic review of mechanical and biological model validation. *Prog. Biomed. Eng.* **2026**, *8*, 022003. [CrossRef] [PubMed]
15. Zanoni, M.; Piccinini, F.; Arienti, C.; Zamagni, A.; Santi, S.; Polico, R.; Bevilacqua, A.; Tesei, A. 3D tumor spheroid models for in vitro therapeutic screening: A systematic approach to enhance the biological relevance of data obtained. *Sci. Rep.* **2016**, *6*, 19103. [CrossRef] [PubMed]
16. Diosdi, A.; Toth, T.; Harmati, M.; Istvan, G.; Schrettner, B.; Hapek, N.; Kovacs, F.; Kriston, A.; Buzas, K.; Pampaloni, F.; et al. HCS-3DX, a next-generation AI-driven automated 3D-oid high-content screening system. *Nat. Commun.* **2025**, *16*, 8897. [CrossRef] [PubMed]
17. Xu, M.; Kong, D.; Sun, S.; Wang, Y.; Su, G.; Zhang, S.; Yan, J.; Han, Z.; Li, J.; Zhang, L. Organoids for disease modeling and treatment: State-of-the-art. *Exp. Hematol. Oncol.* **2026**, *15*, 10. [CrossRef] [PubMed]
18. Verma, V.; Kumar, D. Artificial intelligence and machine learning in drug discovery: From lead discovery to clinical validation (2020–2025). *Lett. Drug Des. Discov.* **2025**, *22*, 100341. [CrossRef]
19. Ocana, A.; Pandiella, A.; Privat, C.; Bravo, I.; Luengo-Oroz, M.; Amir, E.; Gyorffy, B. Integrating artificial intelligence in drug discovery and early drug development: A transformative approach. *Biomark. Res.* **2025**, *13*, 45. [CrossRef] [PubMed]
20. Buterez, D.; Janet, J.P.; Kiddle, S.J.; Oglic, D.; Lió, P. Transfer learning with graph neural networks for improved molecular property prediction in the multi-fidelity setting. *Nat. Commun.* **2024**, *15*, 1517. [CrossRef] [PubMed]

21. Cheng, S.; Li, Y.; Yu, C.; Deng, Z.; Huang, J.; Zhang, Z. 3D bioprinted tumor-vessel-bone co-culture scaffold for breast cancer bone metastasis modeling and drug testing. *Chem. Eng. J.* **2023**, *476*, 146685. [CrossRef]
22. Dozzo, A.; Chullipalliyalil, K.; McAuliffe, M.; O'Driscoll, C.M.; Ryan, K.B. Nano-Hydroxyapatite/PLGA Mixed Scaffolds as a Tool for Drug Development and to Study Metastatic Prostate Cancer in the Bone. *Pharmaceutics* **2023**, *15*, 242. [CrossRef] [PubMed]
23. He, J.; Chen, C.; Chen, L.; Cheng, R.; Sun, J.; Liu, X.; Wang, L.; Zhu, C.; Hu, S.; Xue, Y.; et al. Honeycomb-Like Hydrogel Microspheres for 3D Bulk Construction of Tumor Models. *Research* **2022**, *2022*, 9809763. [CrossRef] [PubMed]
24. Zhang, X.-R.; Wei, B.; Jiang, B.-H.; Ren, W.-H. The pre-metastatic niche: Mechanisms, heterogeneity, and therapeutic opportunities. *Mol. Cancer* **2026**, *25*, 117. [CrossRef] [PubMed]
25. Hernandez, R.K.; Wade, S.W.; Reich, A.; Pirolli, M.; Liede, A.; Lyman, G.H. Incidence of bone metastases in patients with solid tumors: Analysis of oncology electronic medical records in the United States. *BMC Cancer* **2018**, *18*, 44. [CrossRef] [PubMed]
26. Gandaglia, G.; Abdollah, F.; Schiffmann, J.; Trudeau, V.; Shariat, S.F.; Kim, S.P.; Perrotte, P.; Montorsi, F.; Briganti, A.; Trinh, Q.; et al. Distribution of metastatic sites in patients with prostate cancer: A population-based analysis. *Prostate* **2014**, *74*, 210–216. [CrossRef] [PubMed]
27. Naffar-Abu Amara, S.; Kuiken, H.J.; Selfors, L.M.; Butler, T.; Leung, M.L.; Leung, C.T.; Kuhn, E.P.; Kolarova, T.; Hage, C.; Ganesh, K.; et al. Transient commensal clonal interactions can drive tumor metastasis. *Nat. Commun.* **2020**, *11*, 5799. [CrossRef] [PubMed]
28. Bhattacharjee, S.; Hamberger, F.; Ravichandra, A.; Miller, M.; Nair, A.; Affo, S.; Filliol, A.; Chin, L.; Savage, T.M.; Yin, D.; et al. Tumor restriction by type I collagen opposes tumor-promoting effects of cancer-associated fibroblasts. *J. Clin. Investig.* **2021**, *131*, e146987. [CrossRef] [PubMed]
29. Kaplan, R.N.; Riba, R.D.; Zacharoulis, S.; Bramley, A.H.; Vincent, L.; Costa, C.; MacDonald, D.D.; Jin, D.K.; Shido, K.; Kerns, S.A.; et al. VEGFR1-positive haematopoietic bone marrow progenitors initiate the pre-metastatic niche. *Nature* **2005**, *438*, 820–827. [CrossRef] [PubMed]
30. Neto, C.G.T.; Giacometti, J.A.; Job, A.E.; Ferreira, F.C.; Fonseca, J.L.C.; Pereira, M.R. Thermal Analysis of Chitosan Based Networks. *Carbohydr. Polym.* **2005**, *62*, 97–103. [CrossRef]
31. Dong, Y.; Ruan, Y.; Wang, H.; Zhao, Y.; Bi, D. Studies on glass transition temperature of chitosan with four techniques. *J. Appl. Polym. Sci.* **2004**, *93*, 1553–1558. [CrossRef]
32. Santos, K.O.; Barbosa, R.C.; da Silva Buriti, J.; Bezerra Junior, A.G.; de Sousa, W.J.B.; de Barros, S.M.C.; De Oliveira, R.J.; Fook, M.V.L. Thermal, chemical, biological and mechanical properties of chitosan films with powder of eggshell membrane for biomedical applications. *J. Therm. Anal. Calorim.* **2019**, *136*, 725–735. [CrossRef]
33. Ghanem, S.N.; Marzouk, M.I.; Tawfik, M.E.; Eskander, S.B. Spectroscopic approaches for structural analysis of extracted chitosan generated from chitin deacetylated for escalated periods. *BMC Chem.* **2025**, *19*, 214. [CrossRef] [PubMed]
34. Chen, S.; Xing, X.; Su, H.; Voll, D.; Xu, X.; Wan, J.; Cui, T.; Schmitt, C.W.; Bräse, S.; Li, P.; et al. Mechanical Programming of PEGDA-β-CD Polyrotaxane-Based Hydrogels via Host–Guest Molecular Recognition. *Adv. Funct. Mater.* **2026**, *36*, e77853. [CrossRef]
35. Maggi, A.; Li, H.; Greer, J.R. Three-dimensional nano-architected scaffolds with tunable stiffness for efficient bone tissue growth. *Acta Biomater.* **2017**, *63*, 294–305. [CrossRef] [PubMed]
36. Kothapalli, C.; Mahajan, G.; Farrell, K. Substrate stiffness induced mechanotransduction regulates temporal evolution of human fetal neural progenitor cell phenotype, differentiation, and biomechanics. *Biomater. Sci.* **2020**, *8*, 5452–5464. [CrossRef] [PubMed]
37. Morgan, E.F.; Keaveny, T.M. Dependence of yield strain of human trabecular bone on anatomic site. *J. Biomech.* **2001**, *34*, 569–577. [CrossRef] [PubMed]
38. Bregoli, C.; Biffi, C.A.; Tuissi, A.; Buccino, F. Effect of trabecular architectures on the mechanical response in osteoporotic and healthy human bone. *Med. Biol. Eng. Comput.* **2024**, *62*, 3263–3281. [CrossRef] [PubMed]
39. Tse, J.M.; Cheng, G.; Tyrrell, J.A.; Wilcox-Adelman, S.A.; Boucher, Y.; Jain, R.K.; Munn, L.L. Mechanical compression drives cancer cells toward invasive phenotype. *Proc. Natl. Acad. Sci. USA* **2012**, *109*, 911–916. [CrossRef] [PubMed]
40. Morgan, E.F.; Unnikrisnan, G.U.; Hussein, A.I. Bone Mechanical Properties in Healthy and Diseased States. *Annu. Rev. Biomed. Eng.* **2018**, *20*, 119–143. [CrossRef] [PubMed]
41. Mukasheva, F.; Adilova, L.; Dyussenbinov, A.; Yernaimanova, B.; Abilev, M.; Akilbekova, D. Optimizing scaffold pore size for tissue engineering: Insights across various tissue types. *Front. Bioeng. Biotechnol.* **2024**, *12*, 1444986. [CrossRef] [PubMed]
42. Porrelli, D.; Abrami, M.; Pelizzo, P.; Formentin, C.; Ratti, C.; Turco, G.; Grassi, M.; Canton, G.; Grassi, G.; Murena, L. Trabecular bone porosity and pore size distribution in osteoporotic patients—A low field nuclear magnetic resonance and microcomputed tomography investigation. *J. Mech. Behav. Biomed. Mater.* **2022**, *125*, 104933. [CrossRef] [PubMed]
43. Oefner, C.; Riemer, E.; Funke, K.; Werner, M.; Heyde, C.-E.; Schoenfelder, S. Determination of anisotropic elastic parameters from morphological parameters of cancellous bone for osteoporotic lumbar spine. *Med. Biol. Eng. Comput.* **2022**, *60*, 263–278. [CrossRef] [PubMed]

44. Borries, M.; Barooji, Y.F.; Yennek, S.; Grapin-Botton, A.; Berg-Sørensen, K.; Oddershede, L.B. Quantification of Visco-Elastic Properties of a Matrigel for Organoid Development as a Function of Polymer Concentration. *Front. Phys.* **2020**, *8*, 579168. [CrossRef]
45. Kapałczyńska, M.; Kolenda, T.; Przybyła, W.; Zajączkowska, M.; Teresiak, A.; Filas, V.; Ibbs, M.; Bliźniak, R.; Łuczewski, L.; Lamperska, K. 2D and 3D cell cultures-a comparison of different types of cancer cell cultures. *Arch. Med. Sci.* **2018**, *14*, 910–919. [CrossRef] [PubMed]
46. Payr, S.; Rosado-Balmayor, E.; Tiefenboeck, T.; Schuseil, T.; Unger, M.; Seeliger, C.; van Griensven, M. Direct comparison of 3D and 2D cultivation reveals higher osteogenic capacity of elderly osteoblasts in 3D. *J. Orthop. Surg. Res.* **2021**, *16*, 13. [CrossRef] [PubMed]
47. Santibáñez, J.F.; Silva, S.; Martínez, J. Soluble factors produced by PC-3 prostate cells decrease collagen content and mineralisation rate in fetal rat osteoblasts in culture. *Br. J. Cancer* **1996**, *74*, 418–422. [CrossRef] [PubMed]
48. Xin, X.; Wu, Y.; Zang, R.; Yang, S.-T. A fluorescent 3D cell culture assay for high throughput screening of cancer drugs down-regulating survivin. *J. Biotechnol.* **2019**, *289*, 80–87. [CrossRef] [PubMed]
49. Park, D.; Son, K.; Hwang, Y.; Ko, J.; Lee, Y.; Doh, J.; Jeon, N.L. High-Throughput Microfluidic 3D Cytotoxicity Assay for Cancer Immunotherapy (CACI-IMPACT Platform). *Front Immunol.* **2019**, *10*, 1133. [CrossRef] [PubMed]
50. Worthington, P.; Drake, K.M.; Li, Z.; Napper, A.D.; Pochan, D.J.; Langhans, S.A. Implementation of a High-Throughput Pilot Screen in Peptide Hydrogel-Based Three-Dimensional Cell Cultures. *SLAS Discov.* **2019**, *24*, 714–723. [CrossRef] [PubMed]
51. Lekkala, V.K.R.; Kang, S.Y.; Liu, J.; Shrestha, S.; Acharya, P.; Joshi, P.; Zolfaghar, M.; Lee, M.; Vanga, M.G.; Jamdagneya, P.; et al. A Pillar/Perfusion Plate Enhances Cell Growth, Reproducibility, Throughput, and User Friendliness in Dynamic 3D Cell Culture. *ACS Biomater. Sci. Eng.* **2024**, *10*, 3478–3488. [CrossRef] [PubMed]
52. Kim, D.G.; Cha, G.D. Extracellular-Matrix-Mimetic Hydrogels by Using Nanomaterials. *Int. J. Mol. Sci.* **2025**, *26*, 4987. [CrossRef] [PubMed]
53. Wang, Y.; Jeon, H. 3D cell cultures toward quantitative high-throughput drug screening. *Trends Pharmacol. Sci.* **2022**, *43*, 569–581. [CrossRef] [PubMed]
54. Wong, C.H.; Siah, K.W.; Lo, A.W. Estimation of clinical trial success rates and related parameters. *Biostatistics* **2019**, *20*, 273–286. [CrossRef] [PubMed]
55. Yang, H.; Li, J.; Wang, Z.; Khutsishvili, D.; Tang, J.; Zhu, Y.; Cai, Y.; Dai, X.; Ma, S. Bridging the organoid translational gap: Integrating standardization and micropatterning for drug screening in clinical and pharmaceutical medicine. *Life Med.* **2024**, *3*, lnae016. [CrossRef] [PubMed]
56. Mysior, M.M.; Simpson, J.C. An automated high-content screening and assay platform for the analysis of spheroids at subcellular resolution. *PLoS ONE* **2024**, *19*, e0311963. [CrossRef] [PubMed]
57. Katz, A.E.; Johnson, M.; Kasselman, L.J.; Ahmed, S.; Srivastava, A.; Grossfeld, D.J.; Renna, H.A.; Li, K.; Reiss, A.B. Differential Cytokine Profiles in Prostate Cancer Under Treatment: Implications for Prognosis and Synergistic Therapy Design. *Cancers* **2026**, *18*, 967. [CrossRef] [PubMed]
58. Mao, C.; Ding, Y.; Xu, N. A Double-Edged Sword Role of Cytokines in Prostate Cancer Immunotherapy. *Front. Oncol.* **2021**, *11*, 688489. [CrossRef] [PubMed]
59. Calì, B.; Agnellini, A.H.R.; Cioccarelli, C.; Sanchez-Rodriguez, R.; Predonzani, A.; Toffolo, G.I.; Viola, A.; Bronte, V.; Arrigoni, G.; Zonta, F.; et al. GM-CSF Nitration Is a New Driver of Myeloid Suppressor Cell Activity in Tumors. *Front Immunol.* **2021**, *12*, 718098. [CrossRef] [PubMed]
60. Siddiqui, J.A.; Partridge, N.C. Physiological Bone Remodeling: Systemic Regulation and Growth Factor Involvement. *Physiology* **2016**, *31*, 233–245. [CrossRef] [PubMed]
61. Shahriari, K.; Shen, F.; Worrede-Mahdi, A.; Liu, Q.; Gong, Y.; Garcia, F.U.; Fatatis, A. Cooperation among heterogeneous prostate cancer cells in the bone metastatic niche. *Oncogene* **2017**, *36*, 2846–2856. [CrossRef] [PubMed]
62. Sulić, J.; Marijanović, I.; Kraljević, M.; Šućur, A.; Kelava, T.; Mikulić, I.; Ćavar, I. Correlation of Cytokine Profiles with Prostate-Specific Antigen and Disease Grade in Prostate Cancer. *Med. Sci. Monit. Basic Res.* **2024**, *30*, e946776. [CrossRef] [PubMed]
63. Dahl-Wilkie, H.; Gomez, J.; Kelley, A.; Manjit, K.; Mansoor, B.; Kanumuri, P.; Pardo, S.; Molleur, D.; Falah, R.; Konakalla, A.R.; et al. Chronic IL-1-Exposed LNCaP Cells Evolve High Basal p62-KEAP1 Complex Accumulation and NRF2/KEAP1-Dependent and -Independent Hypersensitive Nutrient Deprivation Response. *Cells* **2025**, *14*, 192. [CrossRef] [PubMed]
64. Thomas-Jardin, S.E.; Kanchwala, M.S.; Jacob, J.; Merchant, S.; Meade, R.K.; Gahnim, N.M.; Nawas, A.F.; Xing, C.; Delk, N.A. Identification of an IL-1-induced gene expression pattern in AR+ PCa cells that mimics the molecular phenotype of AR−PCa cells. *Prostate* **2018**, *78*, 595–606. [CrossRef] [PubMed]
65. Kumar, A.; Taghi Khani, A.; Sanchez Ortiz, A.; Swaminathan, S. GM-CSF: A Double-Edged Sword in Cancer Immunotherapy. *Front. Immunol.* **2022**, *13*, 13–2022. [CrossRef] [PubMed]
66. Han, Y.; Wang, Y.; Lv, T.; Yang, Q.; Cheng, D.; Li, J.; Wang, W.; Huang, J.; Peng, X. Effect of colony-stimulating factor in the mechanism of bone metastasis development (Review). *Oncol. Rep.* **2024**, *52*, 1–12. [CrossRef] [PubMed]

67. Kim, T.H.; Oh, S.Y.; Kim, Y.S.; Lee, M.K.; Kim, H.S.; Myung, S.C. Granulocyte macrophage colony-stimulating factor may modulate the post-transcription pathway of interleukin-6 expression in prostate carcinoma cells. *J. Korean Med. Sci.* **2008**, *23*, 94–97. [CrossRef] [PubMed]
68. Akimoto, S.; Okumura, A.; Fuse, H. Relationship Between Serum levels of Interleukin-6, Tumor Necrosis Factor-α and Bone Turnover Markers in Prostate Cancer Patients. *Endocr. J.* **1998**, *45*, 183–189. [CrossRef] [PubMed]
69. Michalaki, V.; Syrigos, K.; Charles, P.; Waxman, J. Serum levels of IL-6 and TNF-α correlate with clinicopathological features and patient survival in patients with prostate cancer. *Br. J. Cancer* **2004**, *90*, 2312–2316. [CrossRef] [PubMed]
70. Zhang, C.; Soori, M.; Miles, F.L.; Sikes, R.A.; Carson, D.D.; Chung, L.W.; Farach-Carson, M.C. Paracrine factors produced by bone marrow stromal cells induce apoptosis and neuroendocrine differentiation in prostate cancer cells. *Prostate* **2011**, *71*, 157–167. [CrossRef] [PubMed]
71. Ketta, M.; Tumová, E. Eggshell structure, measurements, and quality-affecting factors in laying hens: A review. *Czech. J. Anim. Sci.* **2016**, *61*, 299–309. [CrossRef]
72. Benavides-Reyes, C.; Folegatti, E.; Dominguez-Gasca, N.; Litta, G.; Sanchez-Rodriguez, E.; Rodriguez-Navarro, A.B.; Faruk, M.U. Research Note: Changes in eggshell quality and microstructure related to hen age during a production cycle. *Poult. Sci.* **2021**, *100*, 101287. [CrossRef] [PubMed]
73. Ajayan, N.; P, S.; U, A.; Soman, S. Quantitative Variation in Calcium Carbonate Content in Shell of Different Chicken and Duck Varieties. *Adv. Zool. Bot.* **2020**, *8*, 1–5. [CrossRef]

Disclaimer/Publisher's Note: The statements, opinions and data contained in all publications are solely those of the individual author(s) and contributor(s) and not of MDPI and/or the editor(s). MDPI and/or the editor(s) disclaim responsibility for any injury to people or property resulting from any ideas, methods, instructions or products referred to in the content.